

# Exclusive Kaon Electroproduction in Hall B at 6 GeV

## **Spokesmen:**

Daniel S. Carman<sup>a</sup>, Kyungseon Joo<sup>b</sup>,  
Gabriel Niculescu<sup>a</sup>, Brian A. Raue<sup>c</sup>

## **Collaborators:**

Stephen P. Barrow<sup>d</sup>, Volker D. Burkert<sup>e</sup>, Larry Dennis<sup>d</sup>,  
Robert Feuerbach<sup>f</sup>, Kenneth Hicks<sup>a</sup>, Franz J. Klein<sup>c</sup>,  
Costy Loukachine<sup>f</sup>, Rakhsha Nasseripour<sup>c</sup>, Si McAleer<sup>d</sup>,  
John McNabb<sup>g</sup>, Mac D. Mestayer<sup>e</sup>, Reinhard A. Schumacher<sup>g</sup>,  
and the CLAS Collaboration

<sup>a</sup>Ohio University, Athens, OH 45701

<sup>b</sup>University of Virginia, Charlottesville, VA 22901

<sup>c</sup>Florida International University, Miami, FL 33199

<sup>d</sup>Florida State University, Tallahassee, FL 32306

<sup>e</sup>Jefferson Laboratory, Newport News, VA 23606

<sup>f</sup>Carnegie Mellon University, Pittsburgh, PA 15213

<sup>g</sup>Catholic University of America, Washington, D.C., 20064

June 6, 2000

## Abstract

We propose to study strangeness electroproduction in Hall B at a beam energy of 6 GeV via the  $ep \rightarrow e'K^+Y$  reaction. The proposed measurements encompass a number of aspects of existing Hall B experiments focusing on strangeness production. These include extending the kinematic range for hyperon production over which the response functions are extracted, the production mechanisms for  $s$ -channel  $N^*$  creation and decay and  $t$ -channel meson exchange are probed, and the induced and transferred polarization components are measured. The data acquired will allow for detailed tests of hadrodynamical models, constituent quark models, and models based on Regge theory. Each of these individual aspects is important to address for a better understanding of the reaction mechanism of open-strangeness production.

While these data are essential to improve existing low-energy theoretical descriptions of the elementary strangeness-production process, the extension of strangeness production studies to higher-beam energies will also help to elucidate the transition from hadronic to quark-gluon degrees of freedom. This will allow for tests of the validity of non-perturbative QCD in these kinematics. Additionally, the higher-energy data will allow for exploration of the wavefunction of the  $s\bar{s}$  quark pair created through the color flux-tube breaking in the intermediate state and possible access to the underlying quark-distribution functions of the proton.

The reaction kinematics at 6 GeV will span  $Q^2$  from 1.5 to 5  $(\text{GeV}/c)^2$ ,  $W$  from 1.6 to 3.0 GeV, and  $|t|$  beyond 5  $(\text{GeV}/c)^2$  using CLAS at maximum magnetic field. This will allow for study of open-strangeness production at energies well above the resonance region while providing substantial overlap with the kinematic coverage at 4 GeV, which spans  $Q^2$  from 1 to 2.5  $(\text{GeV}/c)^2$ ,  $W$  from 1.6 to 2.4 GeV, and  $|t|$  up to 3  $(\text{GeV}/c)^2$ .

This proposal shows the importance of extending the current Jefferson Laboratory strangeness physics program to 6 GeV while demonstrating the experimental feasibility of the program, both from the standpoint of our detailed analysis of the existing lower-energy CLAS data at 2.4 and 4.0 GeV, as well as through our understanding of CLAS performance from a test run at 5.56 GeV. This proposal is based on the Letter of Intent LOI-99-002 reviewed by PAC-15 and the proposal PR-99-110 reviewed by PAC-16.

# Contents

<b>1</b>	<b>Introduction</b>	<b>1</b>
<b>2</b>	<b>Structure-Function Separation</b>	<b>4</b>
2.1	Introduction . . . . .	4
2.2	$L/T$ Separations with CLAS . . . . .	5
2.3	CLAS Cross-Section Analysis . . . . .	9
<b>3</b>	<b>Hyperon Polarization</b>	<b>10</b>
3.1	Introduction . . . . .	10
3.2	Single-Polarization Formalism . . . . .	11
3.3	Double-Polarization Formalism . . . . .	12
3.4	CLAS Polarization Analysis . . . . .	15
<b>4</b>	<b>Hyperon Production Mechanisms</b>	<b>21</b>
4.1	Hyperon Cross Sections . . . . .	21
4.2	$N^* \rightarrow KY$ Physics . . . . .	23
<b>5</b>	<b>Theoretical Approaches</b>	<b>26</b>
5.1	Hadrodynamical Models . . . . .	26
5.2	Regge-Exchange Models . . . . .	27
5.3	Quark Models . . . . .	29
5.3.1	Quark-Pair Creation . . . . .	29
5.3.2	Quark-Distribution Functions . . . . .	31
<b>6</b>	<b>Performance of CLAS at 6 GeV</b>	<b>33</b>
6.1	Electron/Pion Separation . . . . .	33
6.2	Charged-Particle Identification . . . . .	34
6.3	Final-State Hyperon Identification . . . . .	37
<b>7</b>	<b>CLAS Acceptance Function</b>	<b>38</b>
<b>8</b>	<b>Experimental Details</b>	<b>40</b>
8.1	Data Binning and Statistical Precision . . . . .	40
8.2	Cross-Section Systematics . . . . .	42
8.3	Polarization Systematics . . . . .	45
<b>9</b>	<b>Summary and Beam Time Request</b>	<b>46</b>
<b>10</b>	<b>Appendix</b>	<b>47</b>
10.1	Response-Function Formalism . . . . .	47
10.2	Hadrodynamic-Model Calculations . . . . .	47
10.3	Elastic Cross Section . . . . .	49
10.4	Simple Quark Model . . . . .	50

# 1 Introduction

We propose to use the CEBAF Large Acceptance Spectrometer (CLAS) to study kaon electroproduction from a hydrogen target at a beam energy of 6 GeV to measure cross sections and single- and double-polarization observables. This experiment has two main goals. The first is to extend the existing Hall B strangeness-physics program [1, 2, 3] within the resonance region. The data collected at 6 GeV are an important complement to the existing program allowing the study of open-strangeness production over the entire resonance region where hadronic degrees of freedom are expected to dominate the process. The 6 GeV data will lead to substantive improvements in the structure-function separations approved at lower energies, as well as study of polarization observables over the entire resonance region. The second goal is to extend these measurements to energies beyond the resonance region where hadrodynamic descriptions of strangeness production are expected to break down and where quark degrees of freedom should be much more manifest. This will allow for detailed tests of non-perturbative QCD. Taken together, these goals will lead to a better overall understanding of the elementary strangeness-production process. This proposal requests 30 days of new beam time at 6 GeV (in addition to the 30 days already scheduled in 2001) to carry out this measurement program.

Below  $W$  of around 2-2.2 GeV, isobaric models utilizing Feynman-graph techniques [4, 5, 6] can describe the existing kaon photo- and electroproduction data reasonably well. These models have a sizeable number of free parameters (such as coupling constants  $g_{K\Lambda N}$  and  $g_{K\Sigma N}$ , and hyperon and kaon form factors) and include any number of intermediate resonances. As such, these models can generally fit the existing experimental results quite well even though, in some cases, the models rely on different underlying mechanisms to match the data. For example, Bennhold [7] can explain recent SAPHIR photoproduction cross sections [8] with the inclusion of a previously unseen  $D_{13}(1960)$  resonance. Saghai [9] can explain the same data by instead adding in off-shell effects within his model. Despite improvements made to the database by recent Jefferson Lab and SAPHIR experiments [8, 10], the data are still relatively sparse, cover a limited range of kinematics, and generally suffer from relatively large experimental uncertainties. Measurements of cross sections and polarization observables over a larger range of kinematics are necessary to test the hadronic-field theories and probe the underlying reaction mechanism.

The lack of data also prevent any serious constraint of QCD-based models [11, 12, 13] that predict the formation and decay properties of participating strange baryons. The  $D_{13}(1960)$  resonance mentioned above is predicted in the quark model of Capstick and Roberts [11]. However, without a clear agreement as to the need for this state in explaining the data, its status will remain in doubt. Data taken during this experiment can be used in two ways to look for  $N^*$  resonances: by constraining the hadrodynamic models that include the resonances or as part of a partial-wave analysis of our angular distributions.

Beyond the resonance region, the proposed measurements will help us to better understand the extent to which quark degrees of freedom control the open-strangeness production process. It is expected that variations of the observables with  $W$  should smooth out as one leaves the resonance region [14]. Indeed, as shall be shown later, preliminary CLAS double-polarization data suggest the lack of a strong  $W$  dependence of the data, perhaps indicating that quark degrees of freedom are already important at lower energies.

Extending the existing hadrodynamic models to higher energies is expected to be quite difficult since the Born terms (non-resonant contributions) increase rapidly as a function of energy. Recent calculations have shown that the contributions from the  $t$ -channel resonances are responsible for the divergence of the cross sections from the model predictions, thus indicating that a Regge propagator should be used instead of the usual Feynman propagator [15]. Recent models based on Regge theory have been fairly successful in describing the existing cross-section data at intermediate energies [16, 17]. Again, the current lack of data has yet to allow for a full investigation into the validity of this approach.

The unique capabilities of CLAS provide an opportunity to make significant contributions to the world's data and thus more fully test the existing models of strangeness production. Utilizing the large two-body and three-body acceptances of CLAS will allow us to efficiently detect the  $e'K^+$  and  $e'K^+p$  final states over a large range of kinematics. The coverage of CLAS for  $p(e, e'K^+)X$  at 6 GeV will span  $Q^2$  from 1.5 to 5  $(\text{GeV}/c)^2$ ,  $W$  from threshold (1.62 GeV) to 3.0 GeV, and  $|t|$  beyond 5  $(\text{GeV}/c)^2$ . Fig. 1 shows the significant improvement in  $Q^2$ ,  $W$ , and  $|t|$  coverage in extending the measurements from 4 to 6 GeV.

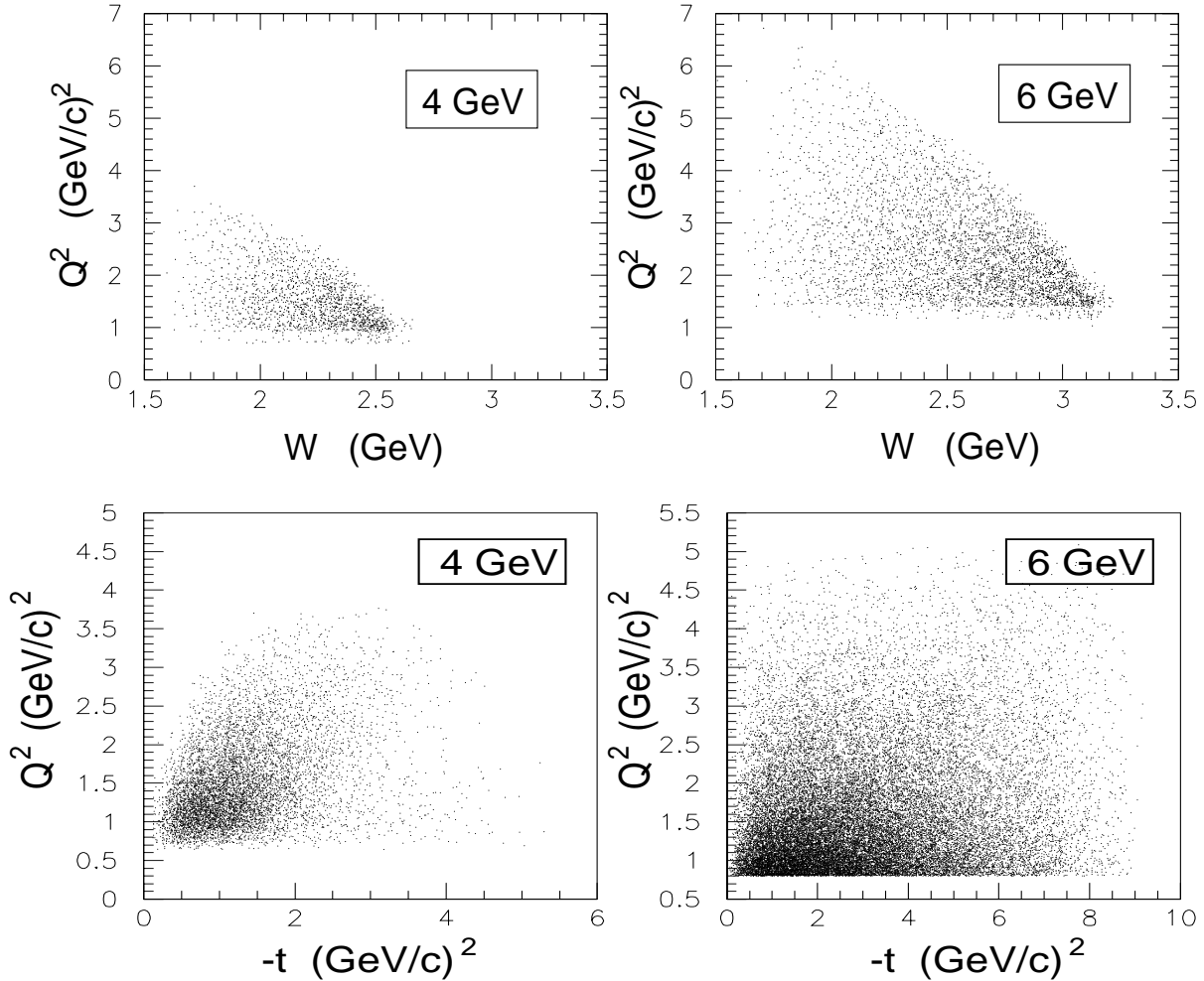


Figure 1: CLAS kinematic coverage for  $p(e, e'K^+)X$  from Monte Carlo in  $Q^2$  vs.  $W$  (top) and  $Q^2$  vs.  $|t|$  (bottom) for both 4 and 6 GeV with full torus magnetic field. The simulation results at both energies agree well with CLAS data measurements.

Combining the 6 GeV data set with the lower-energy measurements should enable important reductions in the uncertainties of the extracted structure functions  $\sigma_L$  and  $\sigma_T$ , as well as the interference terms  $\sigma_{TT}$  and  $\sigma_{TL}$ . CLAS is the only device in the world that allows for measurements of the structure functions over such a broad range of  $Q^2$ ,  $W$ , and  $t$ , and will thus lead to stringent tests of the theoretical predictions.

The use of a polarized-electron beam and utilizing the self-analyzing nature of the hyperon weak decays, allows us to look at various spin characteristics of the reaction through single- and double-polarization measurements. Within the resonance region, polarization data is expected to provide sensitive tests of models of strong-interaction dynamics and represents an essential ingredient in extending our theoretical understanding. In addition, hyperon polarization data may shed light on the quantum numbers of the  $s\bar{s}$  pair created in the intermediate state.

The large acceptance of CLAS allows for study of the reaction over varying kinematical regions where the relative importance of the  $s$ ,  $t$ , and  $u$  reaction channels will vary. By emphasizing specific channel processes we can limit the intermediate baryonic or mesonic exchanges involved in the reaction, which in turn, simplifies our understanding of the results. In this vein, we can study  $s$ -channel processes that specifically include or exclude the  $\Delta$  since we have an automatic isospin filter through selection of either the  $K\Lambda$  or  $K\Sigma$  final state.

In the following sections of this proposal, we will discuss the specific measurements of our program. These include: 1). Extraction of the  $p(e, e'K^+)$  structure functions  $\sigma_T$  and  $\sigma_L$  via a Rosenbluth-type separation and extraction of  $\sigma_{TT}$  and  $\sigma_{TL}$  via a fit to the  $\phi_K^*$ -dependence of the cross sections and 2). Measurement of polarization observables including the fifth response function  $\sigma_{TL'}$  and the induced and transferred hyperon polarizations. These measurements will allow the study of hyperon production and decay mechanisms, the search for missing  $N^*$  resonances predicted to decay to strange final states, and the search for indications of the onset of quark degrees of freedom. While this experimental program is ambitious in its measurement goals, it is important to stress that a full understanding of the kaon-electroproduction process requires all of these measurements. Studying the trends of all observables with increasing beam energy can provide a critical test of the underlying assumptions used in current models of kaon electroproduction.

## 2 Structure-Function Separation

### 2.1 Introduction

The general form for the differential cross section for the exclusive kaon electroproduction reaction is given by the product of the virtual photon flux factor  $\Gamma_v$  and the  $\gamma^*p \rightarrow K^+Y$  virtual photo-absorption differential cross section  $d\sigma_v/d\Omega_K^*$ . With the momenta and angles of the particles involved in the reaction defined in Fig. 2, the most general form for the  $p(e, e'K^+)$  differential cross section, averaging over the spins of all reaction participants, can be expressed in terms of the virtual photon polarization parameter  $\epsilon$ , the kaon azimuthal angle  $\phi_K^*$ , and the kaon structure functions  $\sigma_i$  as:

$$\sigma_0 \equiv \frac{d\sigma_v}{d\Omega_K^*} = \sigma_T + \epsilon\sigma_L + \epsilon\sigma_{TT} \cos 2\phi_K^* + \sqrt{\epsilon(\epsilon+1)/2} \sigma_{TL} \cos \phi_K^*. \quad (1)$$

In general, extraction of the separated  $L$  and  $T$  cross sections and the  $TT$  and  $TL$  interference terms will allow for increased understanding of the underlying reaction mechanism. These separate terms provide sensitivity to the prescription for establishing current conservation in electroproduction models, especially the combination of the non-gauge invariant terms involving the electric proton and kaon form factors.

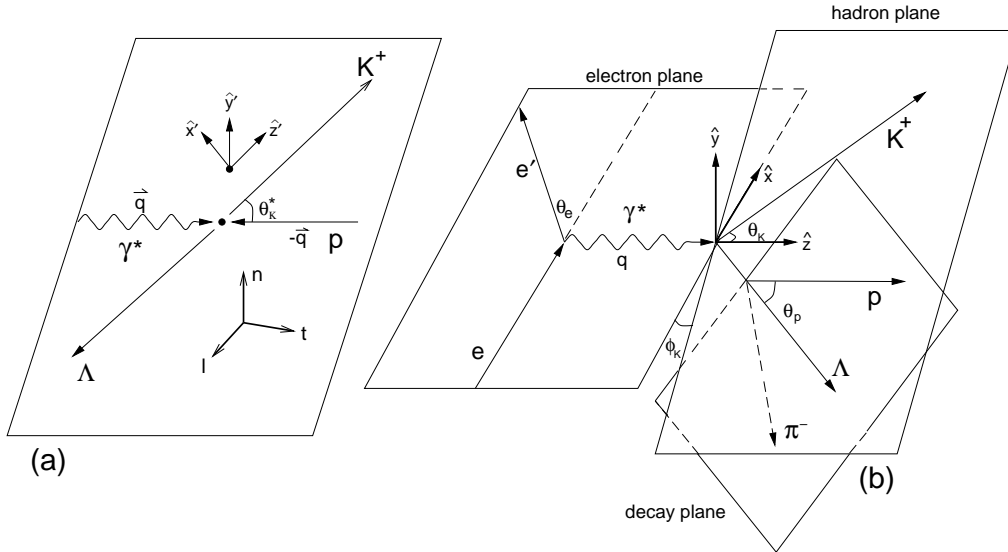


Figure 2: Kinematics for  $K\Lambda$  electroproduction showing angles and polarization axes in (a) the center-of-mass and (b) laboratory coordinate systems.

The four structure functions,  $\sigma_T$ ,  $\sigma_L$ ,  $\sigma_{TT}$ , and  $\sigma_{TL}$ , can be determined as a function of the kinematic variables  $Q^2$ ,  $W$ , and  $t$ .  $\sigma_T$  and  $\sigma_L$  are extracted by comparing measurements at different values of beam energy, and thus different values of  $\epsilon$ , while keeping  $Q^2$ ,  $W$ , and  $t$  fixed. This “Rosenbluth”-type separation is done most precisely for large  $\epsilon$  coverage.  $\sigma_{TT}$  and  $\sigma_{TL}$  are extracted from a fit to the  $\phi_K^*$  dependence of the cross section, resulting in a complete separation of the four structure functions.

## 2.2 $L/T$ Separations with CLAS

At the present time there are only two published experimental results attempting to perform an  $L/T$  separation for kaon electroproduction, and both were done at low  $t$ . The first measurement came from Bebek [18] over 20 years ago. This separation was severely limited by systematic uncertainties at  $\approx 70\%$  of the  $\sigma_L/\sigma_T$  ratio. Recent results from Hall C experiment E93-018 [10] are shown in Fig. 3 at different  $Q^2$  for fixed  $W$  and  $t$  as a function of  $\epsilon$ . Overlaid is the best least-squares fit for  $\sigma_T + \epsilon\sigma_L$ . E93-018 was able to control point-to-point random uncertainties to the 2-3% level, which resulted in a systematic error on the ratio  $R = \sigma_L/\sigma_T$  in the range from 17% to 45% depending on the kinematic bin studied. The fractional error on  $R$  depends on the value of  $R$  as well as on the  $\epsilon$  spread of the fitted data. The specific value of the ratio is sensitive to the spin and transverse momentum of the object that absorbs the virtual photon.

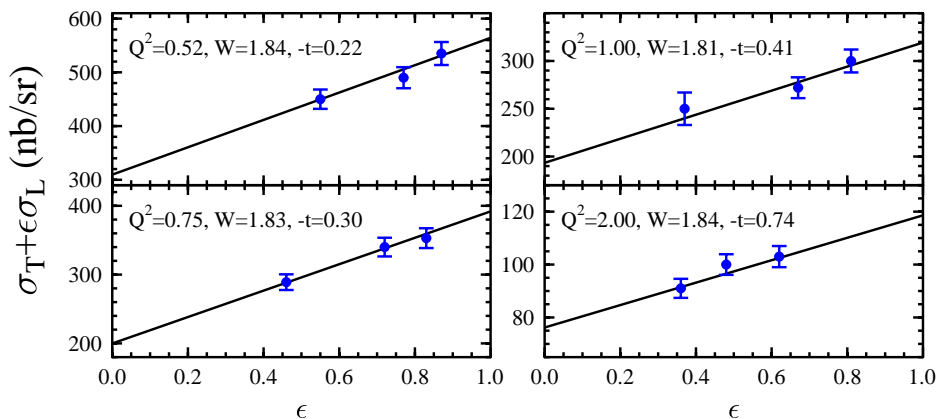


Figure 3: Unseparated  $\sigma_T + \epsilon\sigma_L$  cross sections as a function of  $\epsilon$  for different bins in  $Q^2$  at fixed  $W$  and  $t$  for E93-018 [10]. The lines represent the best least-squares fit for  $\sigma_T$  and  $\sigma_L$  extracted from the data after combining data sets from multiple beam energies (and hence different  $\epsilon$  values).

In Fig. 4, the extracted value of the ratio  $R$  from E93-018 and the Bebek data is shown along with two recent hadrodynamical calculations [7, 19]. These calculations use phenomenological fits of previous world data to extract coupling constants and relevant form factors. The estimated uncertainty in the theoretical predictions are 10 to 15%. Also included in Fig. 4 is the prediction of the model based on Regge-ized  $t$ -channel  $K$  and  $K^*$  exchanges from Guidal [16]. Each of these calculations show essentially the same trend of a dominant longitudinal component at small  $Q^2$  with a gradual fall off of the  $L/T$  ratio with increasing  $Q^2$ . However, the data end at  $Q^2=2$  (GeV/c) $^2$ . This proposed measurement would extend the  $Q^2$  range of the existing data by a factor of two to 4 (GeV/c) $^2$  with expected uncertainties as shown in Fig. 4. It is also important to stress that these data would double the  $t$  range of the  $L$  and  $T$  separated cross sections (see below).

Combining the 6 GeV data set with the lower-energy measurements should enable important reductions in the uncertainties of the  $\sigma_T$  and  $\sigma_L$  structure-function separations already underway in Hall B. These improvements are the result of measurements at additional points in  $\epsilon$ . Increasing the  $\epsilon$  range reduces the uncertainties in the Rosenbluth fit. Additionally, increasing the maximum beam energy from 4 GeV to 6 GeV increases the  $Q^2$  range of the

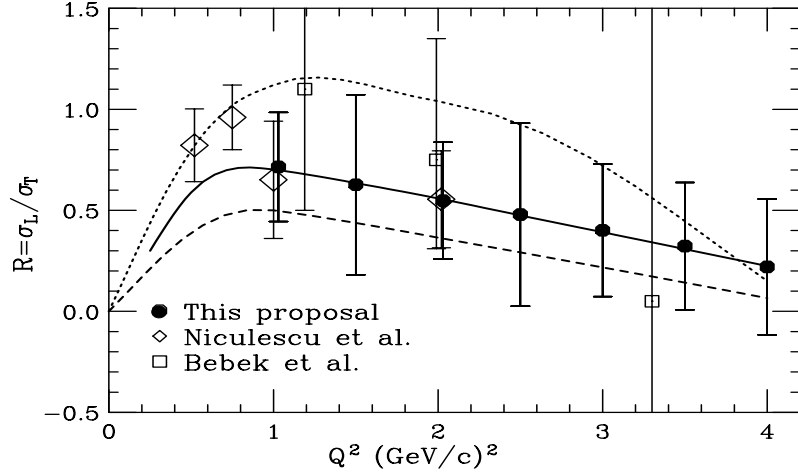


Figure 4: The ratio  $R = \sigma_L/\sigma_T$  for  $ep \rightarrow e'K^+\Lambda$  at  $W = 1.84$  GeV from Refs. [10, 20] at low  $t$  with hadrodynamic calculations from Ref. [7] (dotted line) and Ref. [19] (dashed line), along with a Regge calculation of the GLV model [16] (solid line). Also shown are the expected uncertainties for this experiment upon inclusion of the 6 GeV measurements. The error bars correspond to point-to-point uncertainties of 6% in the cross-section measurements.

extractions from 2 to 4  $(\text{GeV}/c)^2$  and increases the  $W$  range of the extractions from 2.4 GeV to 3.0 GeV. Fig. 5 shows how the range in  $\epsilon$  is expanded as a function of  $Q^2$  by the addition of data at 6 GeV for different values of  $W$ . Finally, increasing the energy range of these measurements will allow for a more broad-range  $t$ -dependent measurement of the  $L/T$  ratio, raising the upper limit of the  $|t|$ -range from 1.5  $(\text{GeV}/c)^2$  to 3  $(\text{GeV}/c)^2$ .

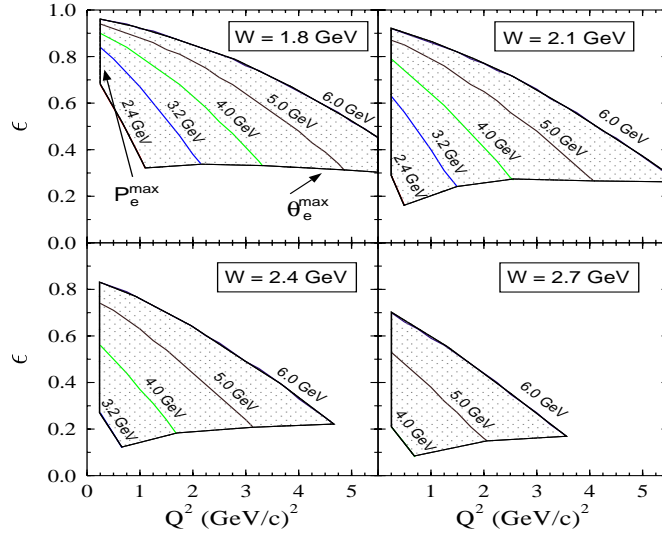


Figure 5: CLAS acceptance (shaded region) of the scattered electron in terms of  $\epsilon$  vs.  $Q^2$  at  $W=1.8$ , 2.1, 2.4, and 2.7 GeV for beam energies in the range from 2.4 to 6.0 GeV.

Table 1 shows a comparison of the  $\epsilon$  range spanned by the data points in the existing lower-energy program and the  $\epsilon$  range spanned with the inclusion of data from CLAS up to 6 GeV. This increased range is important to reduce the systematic uncertainties associated with the Rosenbluth procedure. To show our expectations regarding the uncertainty in the

data analysis, we include here an estimation of the uncertainties associated with our  $L/T$  extraction. A discussion of the expected point-to-point and absolute cross-section uncertainties is contained in Section 8.2. For the current study, we assumed cross-section values from the GLV model [16]. These cross-section points were smeared by a relative point-to-point systematic uncertainty of 6% (expected to be a conservative estimate) and a  $\sigma_T + \epsilon\sigma_L$  fit of the simulated data was done. The fit results provide an estimate of the uncertainty in the separated cross sections and the value of  $R$ . The results of our study are included in Table 2 and shown in Fig. 4.

$W$ (GeV)	$Q^2$ (GeV <sup>2</sup> )	$\epsilon$ Range 1 2.4-4.5 GeV	$\epsilon$ Range 2 2.4-6.0 GeV	$W$ (GeV)	$Q^2$ (GeV <sup>2</sup> )	$\epsilon$ Range 1 2.4-4.5 GeV	$\epsilon$ Range 2 2.4-6.0 GeV
1.8	1.0	0.37–0.85	0.37–0.92	2.1	1.0	0.40–0.73	0.40–0.86
	1.5	0.53–0.79	0.53–0.89		1.5	0.53–0.64	0.53–0.82
	2.0	0.63–0.72	0.63–0.85		2.0	0.41–0.55	0.41–0.77
	2.5	0.52–0.63	0.52–0.81		2.5	0.28–0.45	0.28–0.72
	3.0	0.41–0.54	0.41–0.76		3.0		0.34–0.66
	3.5	0.36–0.45	0.36–0.71		3.5		0.38–0.59
	4.0		0.34–0.65		4.0		0.28–0.52
2.4	1.0	0.37–0.52	0.37–0.76	2.7	1.0		0.21–0.59
	1.5	0.24–0.41	0.24–0.70		1.5		0.27–0.52
	2.0		0.30–0.64		2.0		0.16–0.44
	2.5		0.34–0.57				
	3.0		0.24–0.49				

Table 1: Comparison of the ranges of  $\epsilon$  spanned by CLAS as a function of  $Q^2$  and  $W$  for the current lower-energy program (including 2.4, 3.2, 4.0, 4.2, and 4.5 GeV) to the coverage including beam energies up to 6 GeV.

For the lower  $Q^2$  bins, Table 2 provides a comparison between uncertainties associated with the Rosenbluth technique for fits with and without the 5 and 6 GeV data added to the data from the existing lower-energy program with beam energies up to 4.5 GeV. The fits for the higher  $Q^2$  bins can only be reasonably performed with inclusion of the higher-energy data. Included in Table 2 are the values of  $\sigma_T$  and  $\sigma_L$  determined by our least-squares fit of the simulated data, along with the associated relative uncertainties in the separated cross-section terms and the  $L/T$  ratio. Clearly the improvement in the results with the higher-energy data is substantial.

It is also important to show the increase in the  $|t|$  range over which the  $L$  and  $T$  separations are possible by adding data at 6 GeV. To this end, Fig. 6 shows the overlap in the  $|t|$  vs.  $Q^2$  CLAS acceptance for beam energies of 2.5, 4.2, and 6.0 GeV for 4 different 100 MeV wide bins in  $W$  (integrating over  $\phi_K^*$ ). For this Monte Carlo study for  $\Lambda$  hyperons, loose fiducial cuts (in lab momenta and angles for both the electron and the kaon) were applied. Finally, the studies were performed looking only at kaons with momenta less than 2 GeV/c (to avoid any issues discussed in Section 6.2 regarding particle identification). These studies indicate that the  $L/T$  separations, including the data at 6 GeV, can be extended to  $|t|$  of about 3 (GeV/c)<sup>2</sup>.

$Q^2$ (GeV <sup>2</sup> )	# Points	$\sigma_T$	$\sigma_L$	$R=\sigma_L/\sigma_T$
1.0	5	147±21	105±30	0.72±0.31
	7	147±20	105±26	0.72±0.27
1.5	5	99±23	62±32	0.62±0.47
	7	99±23	62±30	0.63±0.45
2.0	4	72±13	39±21	0.54±0.38
	6	72±10	39±15	0.55±0.29
2.5	3	56±32	27±55	0.49±1.3
	5	56±13	27±19	0.48±0.45
3.0	3	46±17	19±36	0.42±0.94
	5	46±7	19±12	0.40±0.33
3.5	2	39±17	12±42	0.31±1.2
	4	39±6	13±11	0.32±0.32
4.0	3	34±5	7±10	0.22±0.34

Table 2: Relative uncertainties on  $\sigma_T$ ,  $\sigma_L$ , and  $R = L/T$ , comparing the lower-energy program to that including data at 5 and 6 GeV for  $W=1.8$  GeV. Cross sections are given in nb/sr.

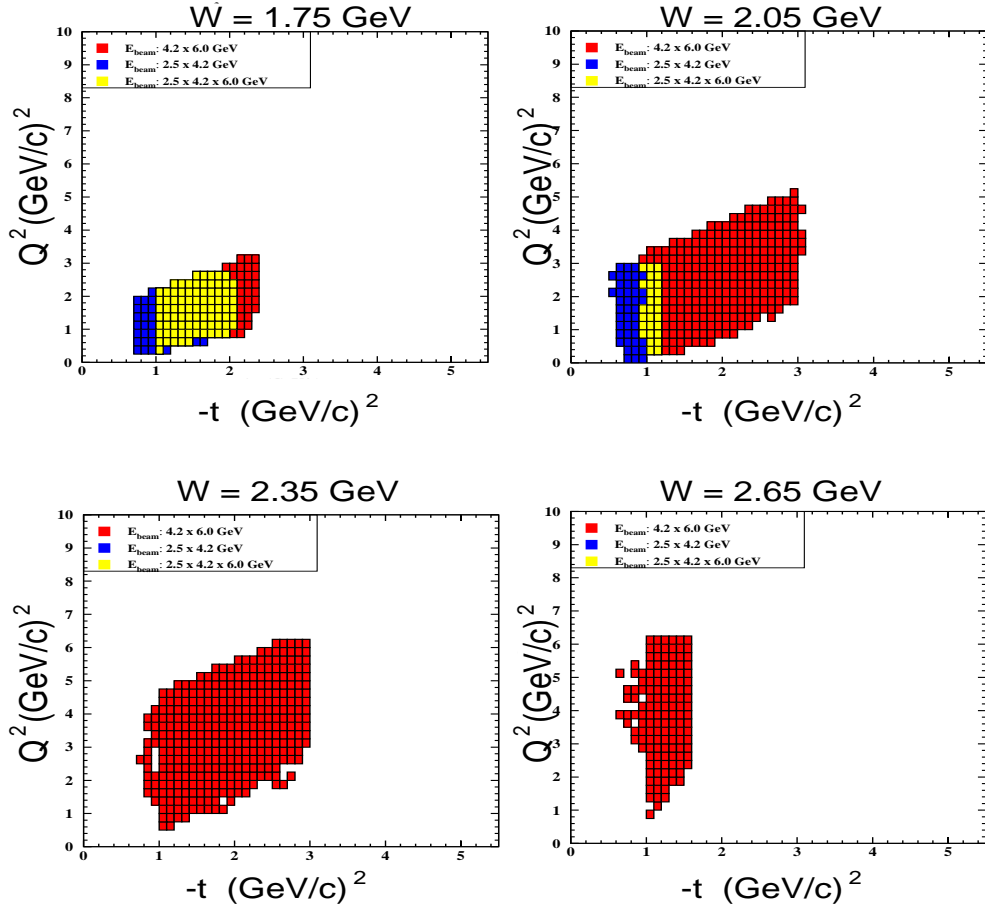


Figure 6: CLAS kinematic overlap for  $p(e, e'K^+)\Lambda$  from Monte Carlo in  $Q^2$  vs.  $|t|$  for beam energies of 2.5, 4.2, and 6.0 GeV.

## 2.3 CLAS Cross-Section Analysis

In this section we provide a brief overview of some of the current preliminary results from our analysis. To begin, we show as a useful consistency check, the present cross-section measurements compared against the existing world data set. In Fig. 7 the cross sections are shown as a function of  $Q^2$ . The most recent data (1999) are shown with the larger stars, while the smaller stars show the 1998 data set results. A dipole fit to guide the eye has been included through the world data set is shown.

In order to match the kinematics accessible to the two-arm spectrometer setups used to acquire most/all of the world data (up to now) for this reaction, only a limited fraction of the data was used:  $W$  around 2.15 GeV (2.0-2.3 GeV) and forward, in-plane kinematics ( $\theta_{\gamma K} \leq 45^\circ$ ). As seen in Fig. 7 the agreement between the present preliminary CLAS measurements and the world data set is good. It is also important to stress that the CLAS data set has many other data points not depicted in Fig. 7 at both lower and higher  $W$  than the slice shown and points at larger  $\theta_{\gamma K}$  angles. Additionally the  $\phi_K^*$  and  $\epsilon$  dependencies of the data can be studied in detail.

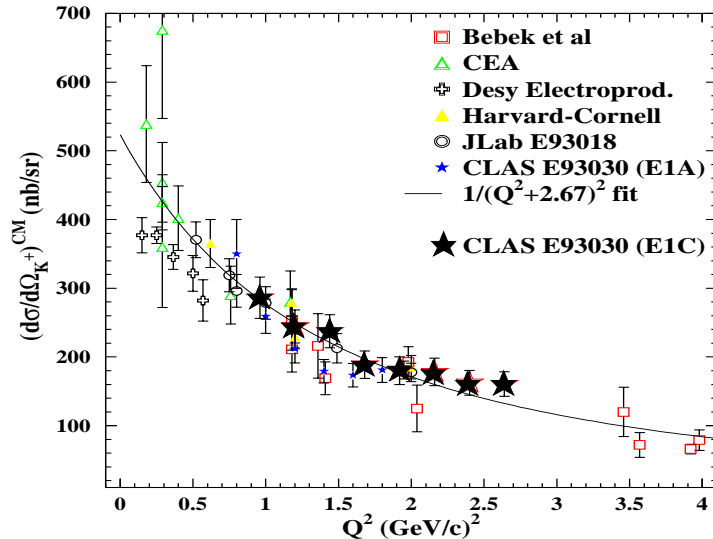


Figure 7:  $Q^2$  dependence of the center-of-mass cross section for the  $p(e, e'K^+)\Lambda$  reaction. The CLAS measurements from E93-030 are preliminary.

In Fig. 8 preliminary CLAS data for the  $\phi_K^*$  dependence of the cross section is shown for  $0.8 \leq Q^2 \leq 1.5$  (GeV/c) $^2$ ,  $1.7 \leq W \leq 2.0$  GeV, for forward-going kaons ( $\theta_{\gamma K} \leq 60^\circ$ ) in the reaction  $p(e, e'K^+)\Lambda$  at 4.247 GeV. The result of a fit of the form  $P_1 + P_2 \cos \phi_K^* + P_3 \cos 2\phi_K^*$  is shown. The fit coefficients can be associated with  $\sigma_T + \epsilon\sigma_L$ ,  $\sigma_{TL}$ , and  $\sigma_{TT}$ . Note that even though each of the points shown in Fig. 8 has relatively large uncertainties of  $\sim 12\%$  (consistent with Table 5), the uncertainty in the parameter  $P_1$  is only of about 4-5%.

Finally we note that another handle we have on the quality of absolute cross-section measurements with CLAS is via the elastic-scattering channel. The results of this analysis are contained in Section 10.3 of the Appendix. The results clearly indicate that for the  $ep$  data, the absolute scale of the cross sections is in excellent agreement (to a level better than 5%) over most of the acceptance region. These results too are quite encouraging for the kaon analysis program.

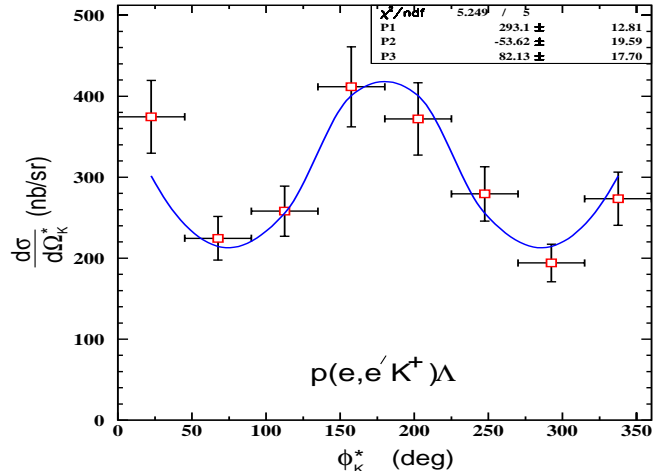


Figure 8: Preliminary CLAS data for the  $\phi_K^*$  dependence of the cross section for the  $p(e, e' K^+) \Lambda$  reaction at 4.247 GeV.

## 3 Hyperon Polarization

### 3.1 Introduction

Because hyperon-production models have been tuned to match the existing cross-section data, there is little variability in their predictions of these quantities. However, predictions of polarization observables have far greater variability and thus the measurement of such observables is an important part of understanding strangeness production. By utilizing a polarized-electron beam and/or measuring the polarization of the final-state hyperon, the spin degrees of freedom can be accessed. By studying their  $W$  dependence (see Section 8.1), polarization observables can be utilized to investigate the contributing hadrons in the intermediate state. For example, different  $s$ -channel resonances are expected to interfere with different strengths depending on the spins involved, and provide a rich response that may be used to isolate contributing states [7].

An attractive feature of the  $\Lambda$  hyperon comes from its self-analyzing nature that allows for determination of its polarization through direct measurement of the angular distribution of the proton from the decay  $\Lambda \rightarrow p\pi^-$ . The decay distribution in the  $\Lambda$  rest frame is of the form:

$$\frac{dN}{d\Omega_p^{RF}} \propto 1 + \alpha P_\Lambda \cos \theta_p^{RF}. \quad (2)$$

In this expression,  $\alpha$  is the weak-decay asymmetry parameter (experimentally determined to be  $0.642 \pm 0.013$  [21]),  $P_\Lambda$  is the  $\Lambda$  polarization, and  $\theta_p^{RF}$  is the decay-proton polar angle in the  $\Lambda$  rest frame relative to the spin-quantization axis. For  $\Sigma^0$  production, the branching ratio is 100% to  $\Lambda\gamma$ . The polarization of this decay  $\Lambda$  is related to the polarization of the  $\Sigma^0$  via  $P_{\Sigma^0} = -3 P_\Lambda$ .

From the decay-proton angular distribution, the average hyperon polarization about each of the three spin axes can be determined. The important measurements to consider in

this program are determinations of the induced (or electron-beam helicity-independent) polarization, and the transferred (or electron-beam helicity-dependent) polarization. The induced and transferred polarizations can be extracted through single-polarization and double-polarization measurements. These measurements will be done over a broad range of kinematics as functions of  $Q^2$ ,  $W$ , and  $t$ .

### 3.2 Single-Polarization Formalism

For this experiment, we will measure single-polarization observables in which either the incident electron or the outgoing hyperon is polarized. These measurements provide access to 6 response functions beyond those accessible through the unpolarized experiments (see Table 7 in Appendix Section 10.1. The experiments made with a polarized-electron beam require detection of only the scattered electron and electro-produced kaon. For this final state, CLAS has an average acceptance of  $\approx 20\%$  at 6 GeV for typical  $Q^2$  and  $W$  values. To measure the induced hyperon polarization, detection of an additional final-state particle, the decay proton, is also required. With this three-body final state, CLAS has an average acceptance of  $\approx 5\%$  at 6 GeV for typical  $Q^2$  and  $W$  values. The discussion of the CLAS two and three-body acceptance at 6 GeV is included in Section 7.

For the case of a polarized-electron beam, the kaon cross section can be written in terms of  $\sigma_0$ , the ‘unpolarized’ cross section from eq(1) (derived from eq(14) with  $\alpha, \beta=0$ ), as:

$$\frac{d\sigma_v}{d\Omega_K^*} = \sigma_0 (1 + hA_{TL'}), \quad A_{TL'} = \frac{K_{CM}}{\sigma_0} c_- {}^s R_{TL'}^{00} \sin \phi_K^*, \quad (3)$$

where  $h$  is the electron-beam helicity. The factor  $K_{CM}$  and the polarization coefficients  $c_i$  are defined in the Appendix Section 10.1. This measurement of the helicity-dependent response term  $A_{TL'}$  allows for sensitivity to the response function  ${}^s R_{TL'}^{00}$  through the cross section difference for the two beam helicity states. This term,  $\sigma_{TL'}$ , is zero in plane-wave calculations. As such, it provides a means of studying the role of final-state interactions as a function of the kinematics. The  $TL'$  response provides sensitivity to the interference between the transverse and longitudinal amplitudes. In fact, the  $TL$  and  $TL'$  responses differ in that they select different combinations of the real or imaginary parts of the interference multipoles [22].

For the case of a polarized hyperon, the kaon cross section can be written as:

$$\frac{d\sigma_v}{d\Omega_K^*} = \sigma_0 \left( 1 + P_{x'}^0 \hat{S}_{x'} \cdot \hat{x}' + P_{y'}^0 \hat{S}_{y'} \cdot \hat{y}' + P_{z'}^0 \hat{S}_{z'} \cdot \hat{z}' \right). \quad (4)$$

The components  $P_{i'}^0$  in this expression correspond to the three induced components of the hyperon polarization and are defined in terms of the hadron-plane (primed) coordinate system defined in Fig. 2. They can be written as:

$$\begin{pmatrix} P_{x'}^0 \\ P_{y'}^0 \\ P_{z'}^0 \end{pmatrix} = \frac{K_{CM}}{\sigma_0} \begin{pmatrix} c_+ R_{TL}^{x'0} \sin \phi_K^* + \epsilon R_{TT}^{x'0} \sin 2\phi_K^* \\ R_T^{y'0} + \epsilon_L R_L^{y'0} + c_+ R_{TL}^{y'0} \cos \phi_K^* + \epsilon R_{TT}^{y'0} \cos 2\phi_K^* \\ c_+ R_{TL}^{z'0} \sin \phi_K^* + \epsilon R_{TT}^{z'0} \sin 2\phi_K^* \end{pmatrix}. \quad (5)$$

Note that because the  $\Lambda$ -spin vector is defined in a coordinate system that is rotating with respect to the laboratory, there are implicit dependencies on  $\theta_K^*$  and  $\phi_K^*$ , in addition to

those shown in eq(5), that have to be taken into account. The terms contributing different response functions in eq(5) can be limited with suitable choice of integration ranges of the angles  $\phi_K^*$  and  $\theta_K^*$ . The large angular range spanned by CLAS is what makes this integration technique possible. If an integration over all  $\phi_K^*$  is performed, which may be essential to reduce the statistical uncertainties, only the  $y$ -component of the induced polarization is non-zero. Additionally, suitable choices of the  $\theta_K^*$  integration range can focus sensitivity of the measurement on an even smaller number of response functions.

Fig. 9 shows the  $y$ -component of the induced  $\Lambda$  polarization (in the electron-plane coordinate system) at 6 GeV as a function of  $W$  for  $Q^2=1.5$  (GeV/c) $^2$  and  $\theta_K^*=90^\circ$  using the hadrodynamical model code of Mart [23], for different model choices and different choices for the  $\Lambda$  and  $KK^*\gamma$  transition form factors. The different curves are explained in Appendix Section 10.2. Each of the different models considered reproduces the existing electroproduction cross-section data reasonably well. The predicted values of  $P_y^0$  are essentially consistent with zero in these kinematics and the variations between the different calculations for  $P_y^0$  are not all that large. However from our analysis of the existing induced polarization data at the lower beam energies (see Section 3.4), it is already apparent that the induced polarization is much larger than these predictions and it will clearly be important to make detailed comparisons of the data to the model predictions over our full kinematic range. Furthermore, these single-polarization data are required to extract the response functions through which the  $P_i^0$  terms are defined.

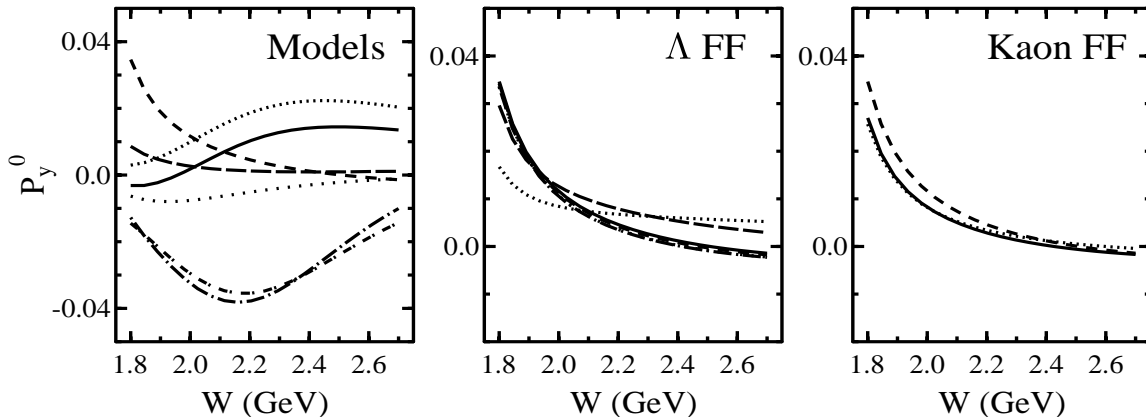


Figure 9:  $P_y^0$  for the reaction  $p(e, e'K^+)\Lambda$  at 6.0 GeV integrated over  $\phi_K^*$  as a function of  $W$  for  $Q^2=1.5$  (GeV/c) $^2$  and  $\theta_K^*=90^\circ$  for different hadrodynamical models (left),  $\Lambda$  form factors (center), and  $KK^*\gamma$  form factors (right). The curves were generated using the hadrodynamical calculation of Mart [23]. The different curves are described in Appendix Section 10.2.

### 3.3 Double-Polarization Formalism

For the double-polarization measurements proposed here, both the beam and recoil hyperon are polarized. Measurements made under these conditions provide access to an additional 5 response functions (see Table 7 in Appendix Section 10.1) that are not accessible through experiments with either polarized beams or polarized recoils alone. In this situation, the cross section of eq(14) becomes:

$$\frac{d\sigma_v}{d\Omega_K^*} = \sigma_0 \left( 1 + hA_{TL'} + P_{x'} \hat{S}_{x'} \cdot \hat{x}' + P_{y'} \hat{S}_{y'} \cdot \hat{y}' + P_{z'} \hat{S}_{z'} \cdot \hat{z}' \right), \quad P_{i'} = P_{i'}^0 + hP_{i'}'. \quad (6)$$

The new polarization components in this expression  $P_{i}'$ , correspond to the three transferred, or helicity-dependent, components of the hyperon polarization and are defined in terms of the hadron-plane (primed) coordinate system defined in Fig. 2. They can be written as:

$$\begin{pmatrix} P_{x'}' \\ P_{y'}' \\ P_{z'}' \end{pmatrix} = \frac{K_{CM}}{\sigma_0} \begin{pmatrix} c_- R_{TL'}^{x'0} \cos \phi_K^* + c_0 R_{TT'}^{x'0} \\ c_- R_{TL'}^{y'0} \sin \phi_K^* \\ c_- R_{TL'}^{z'0} \cos \phi_K^* + c_0 R_{TT'}^{z'0} \end{pmatrix}, \quad (7)$$

where the parameter  $K_{CM}$  and the polarization coefficients  $c_i$  are defined in Appendix Section 10.1.

The terms contributing different response functions in eq(7) can again be limited with suitable choice of integration ranges of the angles  $\phi_K^*$  and  $\theta_K^*$ . If an integration over all  $\phi_K^*$  is performed only the  $x$  and  $z$ -components of the transferred polarization are non-zero. For this situation, sensitivity to the different response functions can be achieved employing a Fourier analysis of the data to take advantage of the different  $\theta_K^*$  dependencies of the response terms.

Fig. 10 shows the  $x$  and  $z$ -components of the transferred  $\Lambda$  polarization (in the electron-plane coordinate system) at 6 GeV as a function of  $\cos \theta_K^*$  for different  $W$  bins at  $Q^2 = 1.0$  (GeV/c)<sup>2</sup> using the hydrodynamic-model code of Mart [23], for different model choices and different choices for the  $\Lambda$  form factor and  $KK^*\gamma$  transition form factor. Again, these calculations show the uncertainties in the underlying response functions through which the polarization components are defined.

Two recent papers have shown for the general case of pseudoscalar meson electroproduction in parallel kinematics that extraction of the  $L/T$  response can be done, in principle, without performing a Rosenbluth separation [24, 25]. For the restrictive case of parallel kinematics, the  $\Lambda$  polarization components can be written as:

$$P_{x'} = c_- \frac{R_{LT'}^{x'0}}{R_T^{00} + \epsilon_L R_L^{00}}, \quad P_{y'} = c_+ \frac{R_{LT'}^{y'0}}{R_T^{00} + \epsilon_L R_L^{00}}, \quad P_{z'} = c_0 \frac{R_{TT'}^{z'0}}{R_T^{00} + \epsilon_L R_L^{00}}. \quad (8)$$

Written in terms of the so-called reduced polarizations,  $\chi_i = P_i/c$ , the following relations for the  $L/T$  response emerge:

$$\chi_x^2 + \chi_y^2 = \frac{R_T^{00} \cdot R_L^{00}}{(R_T^{00} + \epsilon_L R_L^{00})^2}, \quad \chi_z^2 = \frac{(R_T^{00})^2}{(R_T^{00} + \epsilon_L R_L^{00})^2}. \quad (9)$$

Thus,

$$\frac{R_L^{00}}{R_T^{00}} = \frac{\chi_x^2 + \chi_y^2}{\chi_z^2} = \frac{1}{\epsilon} \left( \frac{1}{\chi_z - 1} \right). \quad (10)$$

In principle, measurement of the  $\Lambda$  polarization components can provide a model-independent relation for the  $L/T$  response. At the least, this type of approach can be used as a consistency check on the experimental data.

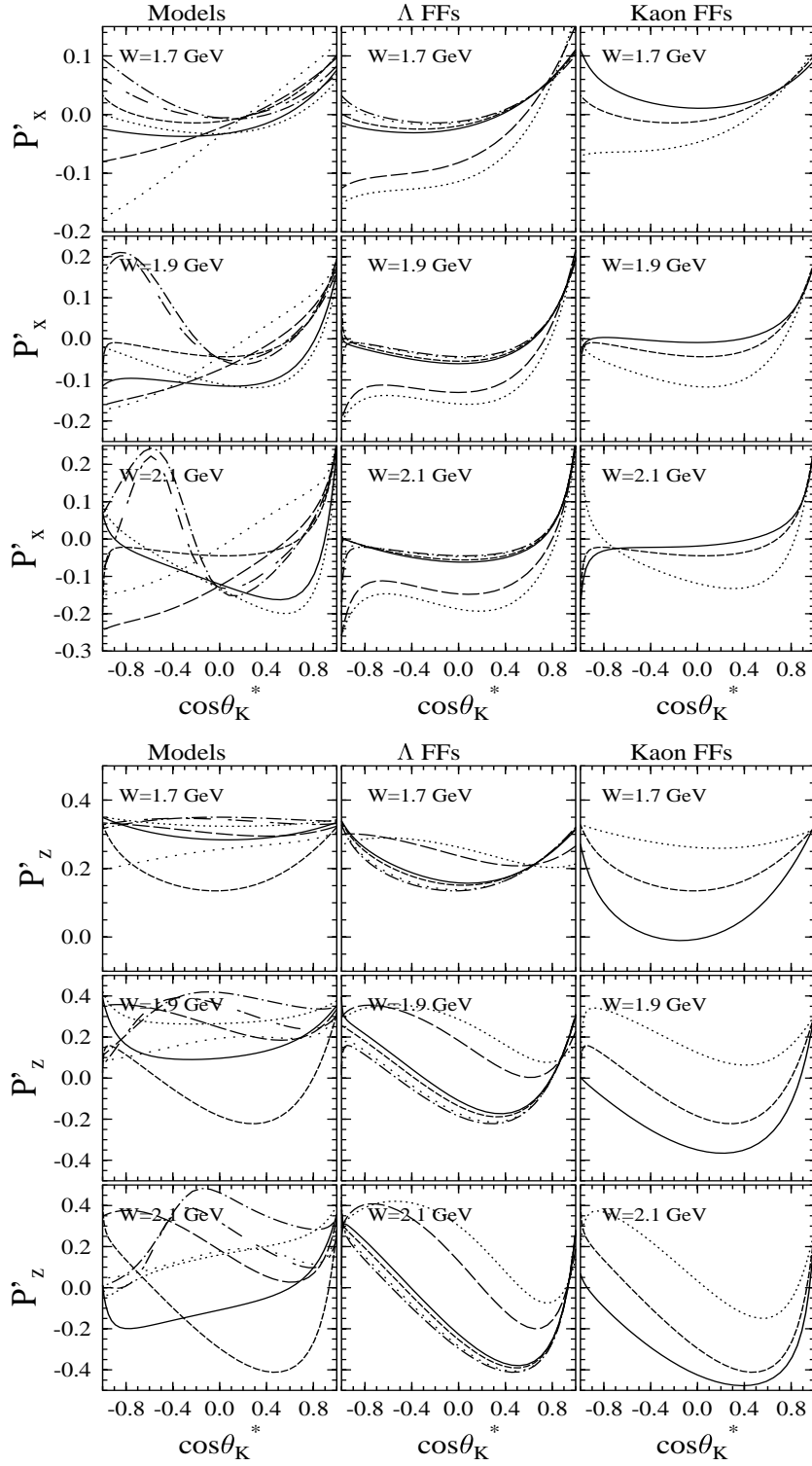


Figure 10:  $P'_x$  and  $P'_z$  for the reaction  $p(e, e'K^+)\Lambda$  at 6.0 GeV integrated over  $\phi_K^*$  for  $W = 1.7, 1.9,$  and  $2.1$  GeV at  $Q^2=1.0$  (GeV/c) $^2$  as a function of  $\cos\theta_K^*$  for different hydrodynamic models (left),  $\Lambda$  form factors (center), and  $KK^*\gamma$  form factors (right). The curves were generated using the hydrodynamic-model code of Mart [23]. The different curves are described in Appendix Section 10.2.

### 3.4 CLAS Polarization Analysis

At the present time the analysis of the hyperon polarization data taken at lower energies is still in a fairly early stage. However significant progress has been made over the past few months. For the induced  $\Lambda$  polarization measurements, the decay-proton yields have been corrected for the combined effects of the CLAS acceptance function and kaon in-flight decays. Preliminary results from analysis of the 4.247 GeV/60% torus-field data set are shown in Figs. 11 and 12. The data presented are summed over all  $Q^2$  and  $\phi_K^*$  and shown with respect to the  $\ell, n, t$  coordinate system defined in Fig. 2.

Fig. 11 shows the acceptance-corrected yields for the longitudinal and transverse spin-quantization axes (defined in Fig. 2). Parity conservation in the electromagnetic interaction requires these distributions to be flat. Present deviations provide a measure of the level of systematic uncertainty in the current analysis.

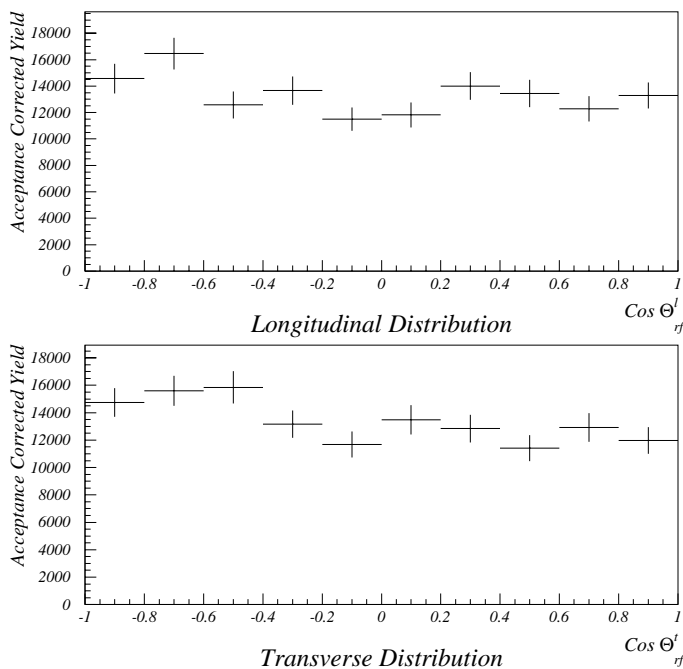


Figure 11: Preliminary CLAS analysis results for the accepted-corrected yields for the  $\Lambda$  decay proton with respect to the  $\ell$  and  $t$  spin-quantization axes for 4.247 GeV data. The yields have been summed over  $Q^2$  and  $\phi_K^*$ .

Fig. 12 shows the normal component of the induced  $\Lambda$  polarization (allowed to be non-zero from parity) for two different  $W$  bins including 4 bins in  $\cos\theta_K^*$ . The data is fit by the functional form  $\sin\theta_K^*(a + b\cos\theta_K^*)$  that takes into account  $L=0,1$  contributions only. These results for the induced  $\Lambda$  polarization are seen at this stage to be entirely consistent with the recent SAPHIR photoproduction data [8]. The forward/backward asymmetry seen has been interpreted as a resonant interference effect from isobar excitations decaying into the  $K\Lambda$  channel. This approach also serves to fit the SAPHIR differential cross section data well over their energy range,  $1.05 \leq E_\gamma \leq 1.75$  GeV.

To better understand the results, it will be important to bin the data in  $W$  as finely as

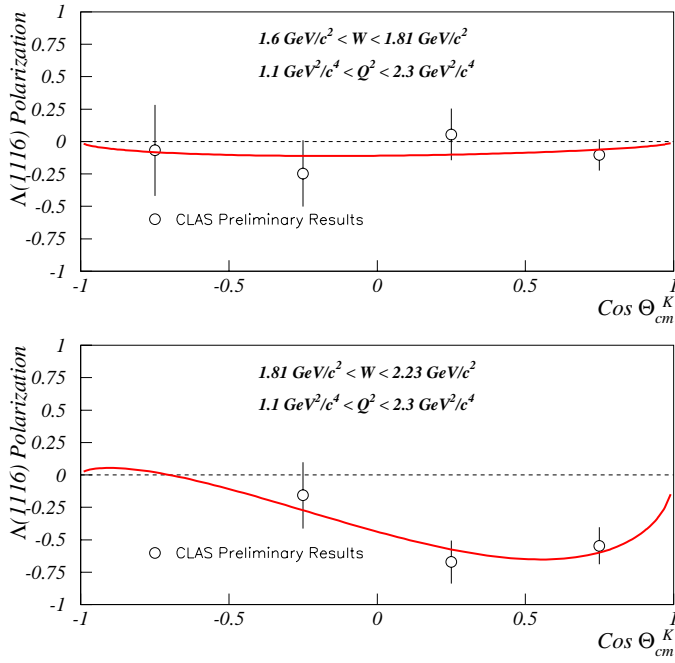


Figure 12: Preliminary CLAS analysis results for the  $\Lambda$  induced polarization  $P_n^0$  for two different  $W$  bins at 4.247 GeV summed over all  $Q^2$  and  $\phi_K^*$ . The data have been fit with a curve including  $L=0,1$  terms explained in the text.

possible to limit the contribution of overlapping resonances. Recent analyses of SAPHIR data around  $W \sim 1900$  MeV have made this quite clear [7]. Data analyzed in the context of isobar models have shown large changes in the predicted hyperon polarization by adding or removing individual resonances. However, from another point of view, it is important to extend these measurements beyond the resonance region (i.e.  $W \geq 2.4$  GeV) where models based on resonant excitation and decay are supplanted by models based on quark-level dynamics, especially if the appropriate basis to describe hyperon polarization is in terms of quarks and not resonance interference.

Like the induced polarization analysis, the transferred polarization analysis has been ongoing for several months. Both programs have a sizeable list of ultimate goals, but already some interesting results of the analysis have come out. Unlike the analysis of the single-polarization data that explicitly requires that the CLAS acceptance to function be included to properly correct the  $\cos \theta_p^{RF}$  distributions, a portion of the double-polarization analysis can proceed by extracting the polarization from the yield asymmetries:

$$A_i = \frac{N^+ - N^-}{N^+ + N^-} = \frac{\alpha \cos \theta_p^{RF} P_i'}{1 + \alpha \cos \theta_p^{RF} P_i^0}, \quad i = \ell, n, t. \quad (11)$$

This asymmetry is formed from the  $\cos \theta_p^{RF}$  yields for the three spin-quantization axes  $\ell$ ,  $n$ , and  $t$  (defined in Fig. 2) gated by the beam-helicity states ( $h = +1$  or  $-1$ ). In this method, the CLAS acceptance function cancels out, assuming that it does not depend on the beam helicity.

In forming these asymmetries and integrating over all  $\phi_K^*$ ,  $P_t^0 = P_\ell^0 = P_n^0 = 0$ . In general, if  $P_i^0 = 0$ , then the corresponding polarization asymmetry is given by  $A_i = \alpha \cos \theta_p^{RF} P_i'$ . If  $P_i' = 0$ , then the corresponding asymmetry must vanish. Thus from parity  $A_n = 0$ , but  $A_\ell$

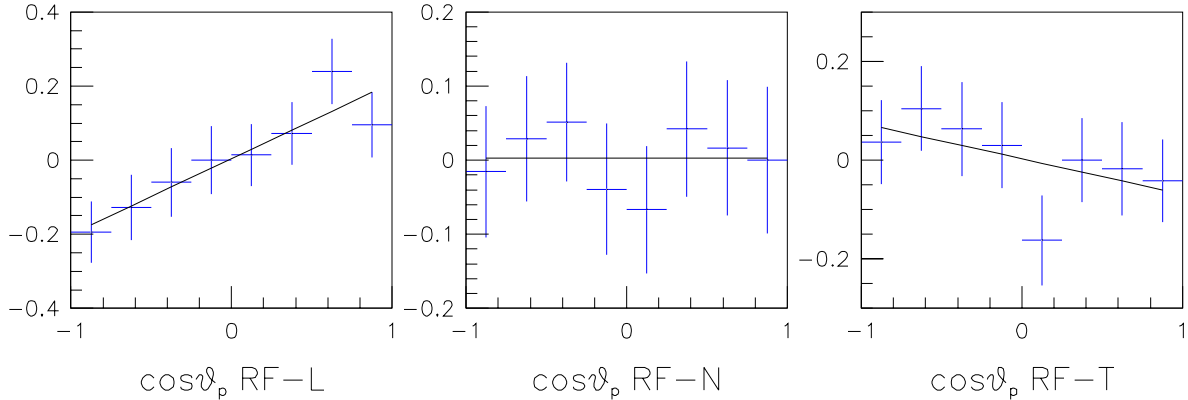


Figure 13: Polarization yield asymmetries for  $\Lambda$  production at 4.247 GeV for a representative bin in  $Q^2$  and  $W$  ( $Q^2=1.6$  (GeV/c) $^2$ ,  $W=1.8$  GeV).

and  $A_t$  can be non-zero and the transferred polarization can be extracted. Fig. 13 shows results of our asymmetry fits at 4.247 GeV/60% field to indicate the quality of our data for  $A_\ell$ ,  $A_n$ , and  $A_t$  in a representative bin of  $Q^2$  and  $W$ .

The results of our preliminary polarization analysis at 4.247 GeV, accounting for the average beam polarization of 0.67, are shown in Figs. 14 and 15 for  $P'_\ell$  and  $P'_t$  as a function of  $Q^2$  for three 300-MeV wide bins of  $W$  (1.75, 2.05, 2.35 GeV) and two bins in  $\cos\theta_K^*$  going back to  $\theta_K^*=90^\circ$ . The widths of these bins was chosen to allow for studies with the smallest bins possible while maintaining reasonable statistical uncertainties.

These data show several interesting trends. First, we note that the transferred polarization is quite sizeable in these kinematics. It also appears to be relatively independent of  $Q^2$  within the size of the current error bars. This effect could arise for a given bin of  $W$  if only a single  $s$ -channel resonance were present (or if a single resonance were dominant). Looking at these data for increasing  $\cos\theta_K^*$  indicates the development of a suppression in  $P'_\ell$ , a result seen in the induced polarization data as well (see Fig. 12). However, the magnitude of  $P'_t$  seems to be increasing slightly with increasing  $\theta_K^*$ .

Fig. 16 shows the data for  $P'_\ell$  and  $P'_t$  integrating over  $Q^2$  as a function of  $W$  for  $\cos\theta_K^*$  bins extending back to  $120^\circ$ . A forward-backward asymmetry is clearly seen in  $P'_\ell$ , consistent with the induced polarization and interpreted as a signature of an interference effect.  $P'_t$  seems relatively flat in these variables. At this point we can also notice that there seems to be no apparent dependence on  $W$  given our current binning choices. We expect that if the hyperon polarization indeed arises from resonance interference effects, the polarization should depend strongly on  $W$ . If this trend continues to hold as our  $W$  bin size decreases (as we combine the remainder of the e1 data set together) and remains for the CLAS  $W$  range spanned at 6 GeV, the immediate conclusion is that our current theoretical models are not describing the dynamics correctly. At the very least, if the polarization trend continues to higher energies, we have clear evidence that quark degrees of freedom may be setting in, even in the resonance region.

Finally, our preliminary extraction of the fifth structure function is shown in Fig 17 as a function of  $\phi_K^*$  for different bins in  $W$  from 4.247 GeV data. This term, shown in eq(3), can be extracted from the yields without incorporating the CLAS acceptance function simply

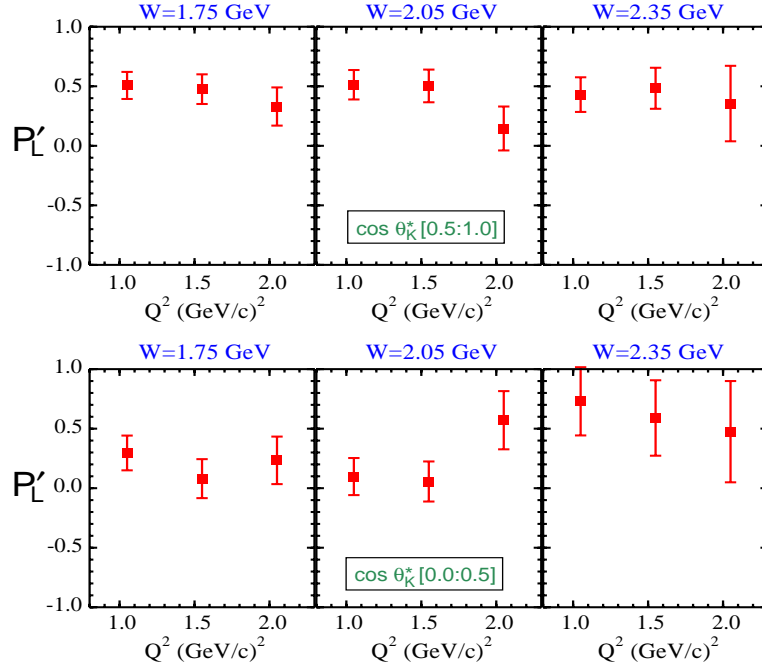


Figure 14: Transferred  $\Lambda$  polarization component  $P'_l$  from preliminary CLAS analysis of 4.247 GeV/60% field data as a function of  $Q^2$  for bins in  $W$  and  $\cos \theta_K^*$ .

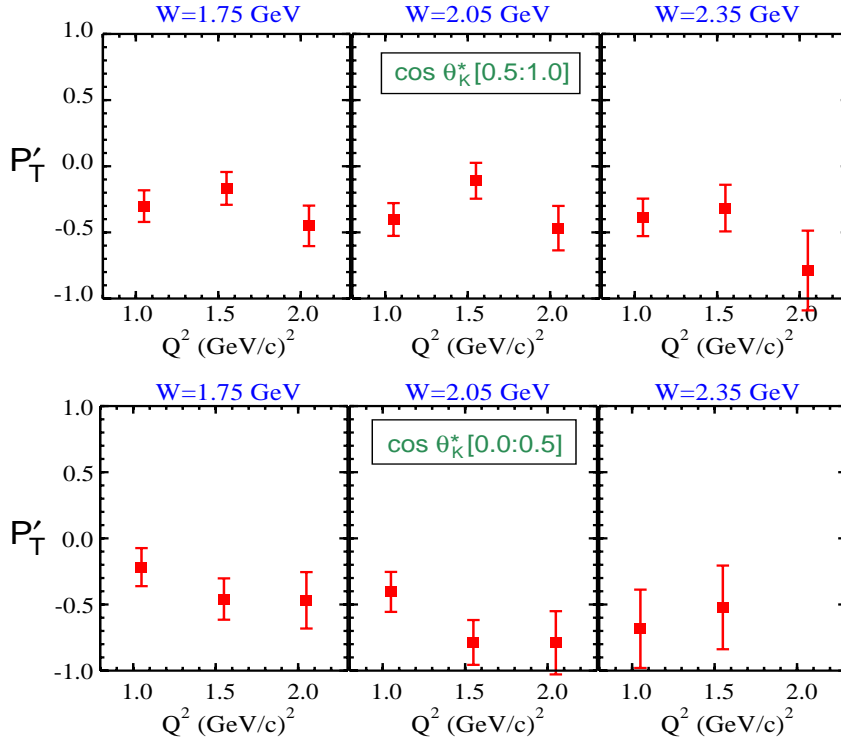


Figure 15: Transferred  $\Lambda$  polarization component  $P'_t$  from preliminary CLAS analysis of 4.247 GeV/60% field data as a function of  $Q^2$  for bins in  $W$  and  $\cos \theta_K^*$ .

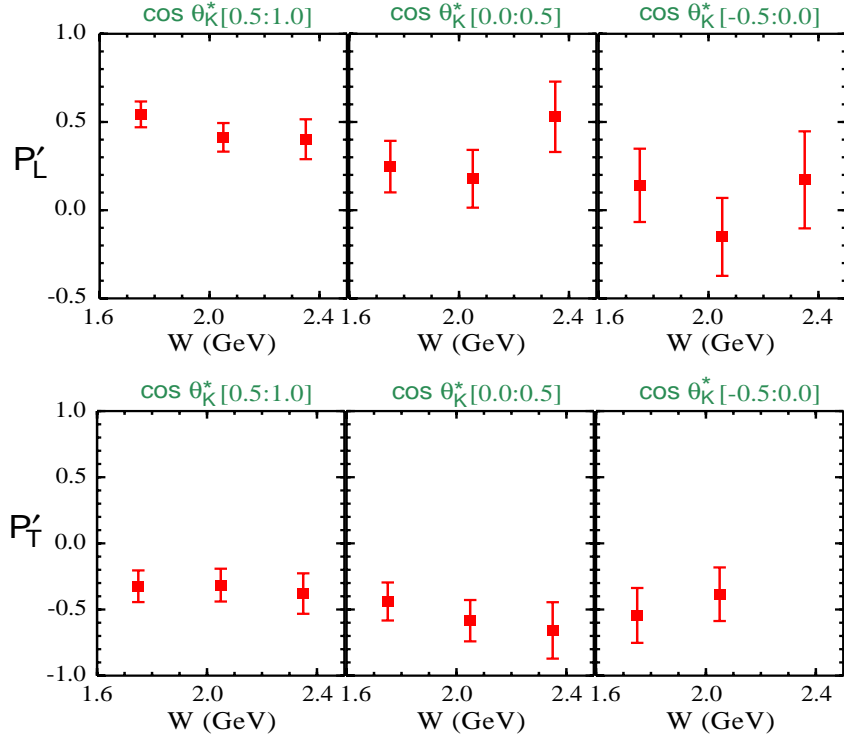


Figure 16: Transferred  $\Lambda$  polarization components  $P'_L$  and  $P'_T$  from preliminary CLAS analysis of 4.247 GeV/60% field data as a function of  $W$  for bins in  $\cos \theta_K^*$  integrated over  $Q^2$ .

by forming the yield asymmetry  $(\sigma^+ - \sigma^-)/(\sigma^+ + \sigma^-)$ , where the sign indicates the helicity state of the electron beam. Again, this term is proportional to  $R_{TL}^{00}$  and provides a means of studying the role of final-state interactions.

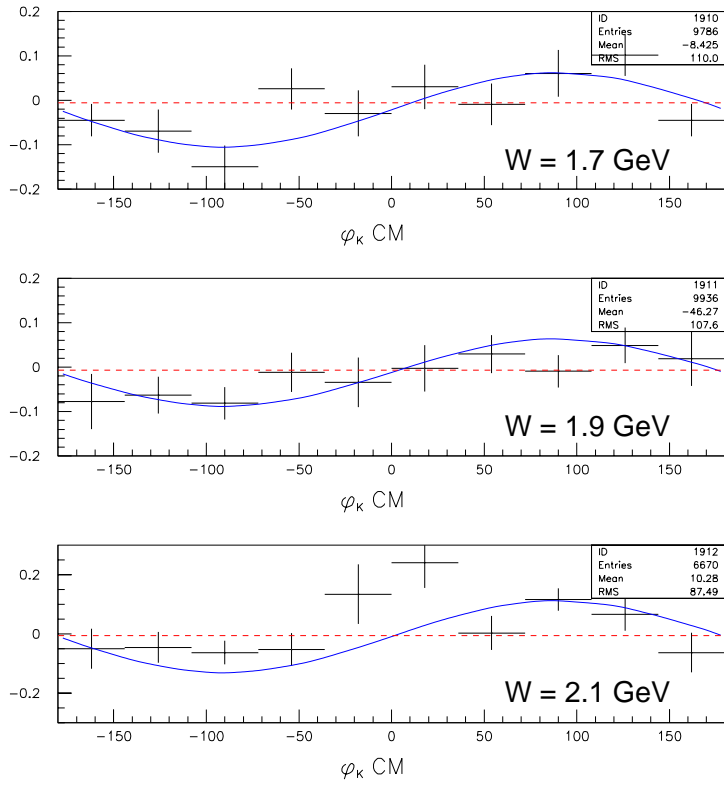


Figure 17: Preliminary CLAS data for the fifth structure function  $A_{TL}'$  as a function of  $\phi_K^*$  for 4.247 GeV for different bins in  $W$  summed over  $Q^2$  and fit with a sine curve.

## 4 Hyperon Production Mechanisms

### 4.1 Hyperon Cross Sections

An important goal of this experiment is to better understand the mechanisms for strange final-state production. One technique to do this is to measure the production ratio of the various final-state hyperons,  $\Lambda$ ,  $\Sigma^0$ ,  $\Lambda(1405)$ ,  $\Sigma(1385)$ , and  $\Lambda(1520)$  as a function of  $Q^2$ ,  $t$ ,  $W$ , and  $\cos\theta_K^*$ . Ratios of hyperon yields should be totally insensitive to a number of sources of systematic uncertainty including dead time and integrated beam current. We can also expect a greatly reduced sensitivity to other important sources of uncertainty including CLAS acceptance, reconstruction efficiencies, and in-flight decays. Furthermore, these ratios have little sensitivity to changes in the experimental conditions thus reducing the systematic uncertainties involved when combining data sets.

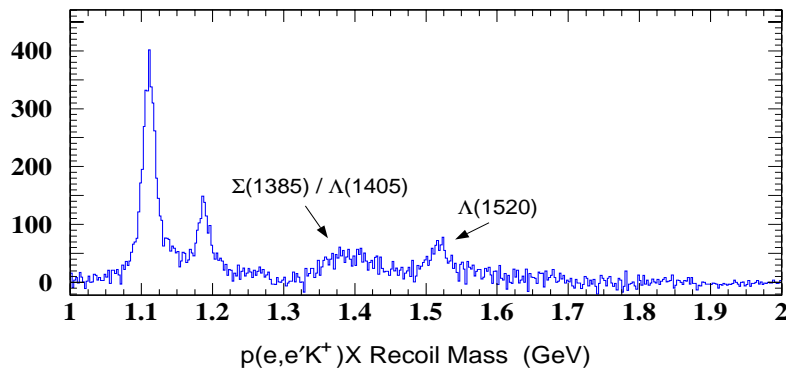


Figure 18: Recoil-mass spectrum for 4 GeV  $p(e, e'K^+)X$  CLAS data with the predominant pion background from misidentified kaons subtracted.

We have been analyzing the existing 2.4 and 4.0 GeV  $e1$  data acquired in 1998 and 1999. A mass spectrum from the 4.0 GeV CLAS data is shown in Fig. 18. At the present stage, we have extracted background-subtracted yields that have been corrected for the CLAS geometric acceptance, kaon in-flight decays, beam-target luminosity, finite bin size effects, and radiative effects. Preliminary analysis of the  $Q^2$  dependence of these data for different  $t$  bins already shows an interesting behavior as seen in Fig. 19.  $\Lambda$  production tends to dominate  $\Sigma^0$  production at small  $t$  and large  $Q^2$ . However the data also indicate that as  $t$  increases,  $\Sigma^0$  production quickly surpasses  $\Lambda$  production. Note that due to statistical limitations, this analysis was performed summing over all  $W$  ( $1.6 \leq W \leq 2.2$  GeV). The  $Q^2$  dependence of these data is expected to show sensitivity to the form factors of the exchanged hadrons. Extensions of the  $KY$  data sets to 6 GeV will allow for a greatly increased range of  $Q^2$  and  $t$  to be spanned. Studying the trends of the data over this increased kinematic range is important to fully test the reaction models.

It is expected that the  $t$ -dependence of the  $\Sigma^0$  to  $\Lambda$  ratio will shed light on possible differences in the exchanged particles for the two final states, as well as differences in the hyperon wavefunctions. The preliminary CLAS analysis results at 2.4 and 4.0 GeV are shown in Fig. 20, which shows the  $\Sigma^0$  to  $\Lambda$  ratio for fixed  $Q^2$  and integrated over  $W$ . Ultimately, one wants to study the  $t$ -dependence of the ratio finely binned in *both*  $Q^2$  and  $W$ . Narrow

bins in  $W$  are required to limit the mass of the exchanged hadron in the intermediate state, and study of the  $Q^2$  dependence of the yields is essential to extract the associated form factors. At the present time, statistical limitations prevent fine binning in either  $Q^2$  or  $W$ . Fig. 21 however shows the  $\Sigma^0/\Lambda$  yield as a function of  $t$  for different  $W^2$  bins (now summing over  $Q^2$ ). The variations of the ratio with  $W^2$  are a clear indication of the different mix of amplitudes in the intermediate state for  $\Sigma^0$  and  $\Lambda$  production. The interest in the analysis is to study the  $t$ -dependent slope for the largest possible range of  $Q^2$ , thus data points at 6 GeV are important in this regard.

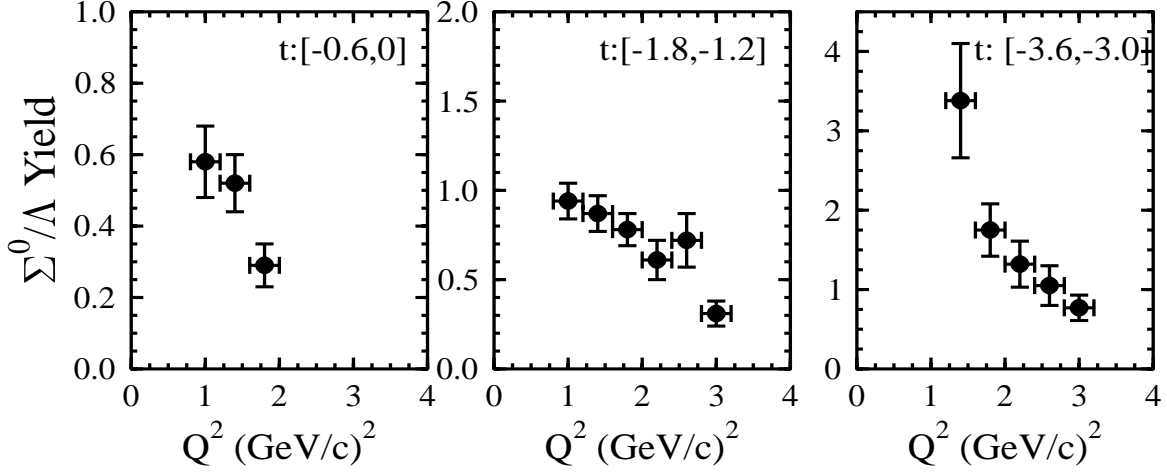


Figure 19: Preliminary CLAS data for hyperon production showing the ratio of corrected yields for  $\Sigma^0$  to  $\Lambda$  production as a function of  $Q^2$  for different  $t$  ranges for 4.0 GeV (87% field) data.

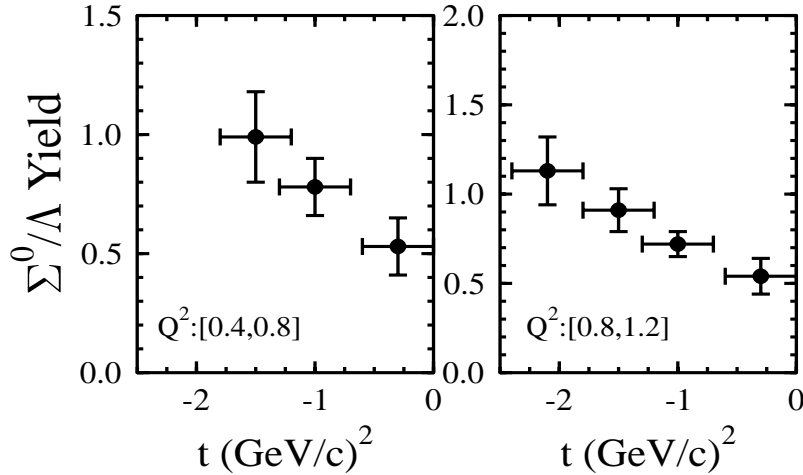


Figure 20: Preliminary CLAS data for hyperon production showing the ratio of corrected yields for  $\Sigma^0$  to  $\Lambda$  production as a function of  $t$  for different  $Q^2$  ranges for 4.0 GeV (60% field) data.

Fig. 22 shows an important preliminary CLAS result for the separate  $\Lambda$  and  $\Sigma$  corrected yields. This figure shows the corrected hyperon yields at 2.4 and 4.0 GeV as a function of  $\cos \theta_K^*$ . The data indicate that  $\Lambda$  production has a much larger  $t$ -channel strength than  $\Sigma^0$  production. As well, considering the shape and heights of the tails, the underlying  $s$ -channel

strengths may be comparable. Our goal is to continue this study over the broader kinematic range spanned by CLAS at 6 GeV.

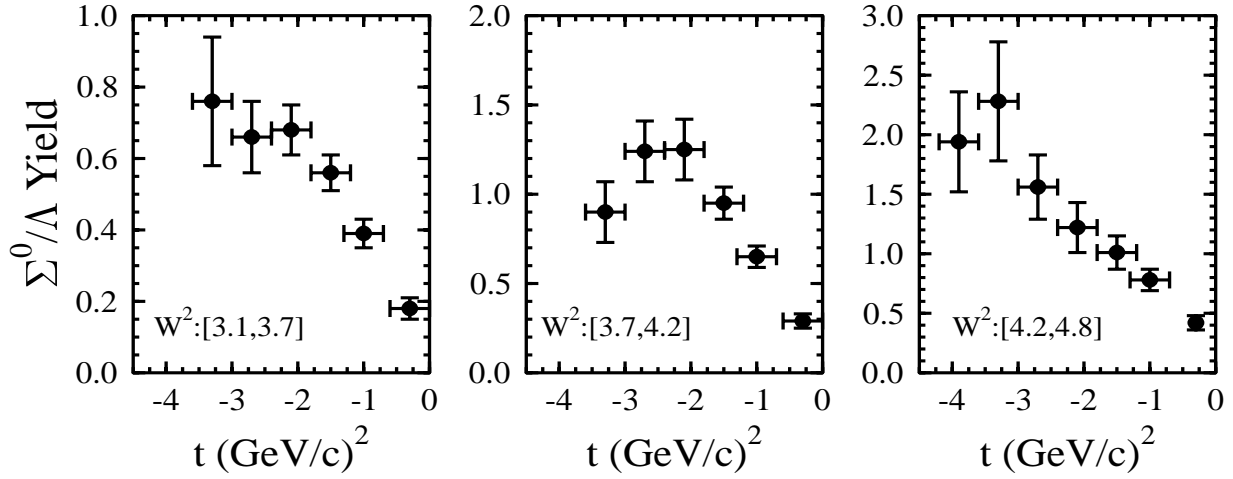


Figure 21: Preliminary CLAS data for hyperon production showing the ratio of corrected yields for  $\Sigma^0$  to  $\Lambda$  production as a function of  $t$  for different  $W^2$  ranges for 4.0 GeV (87% field) data.

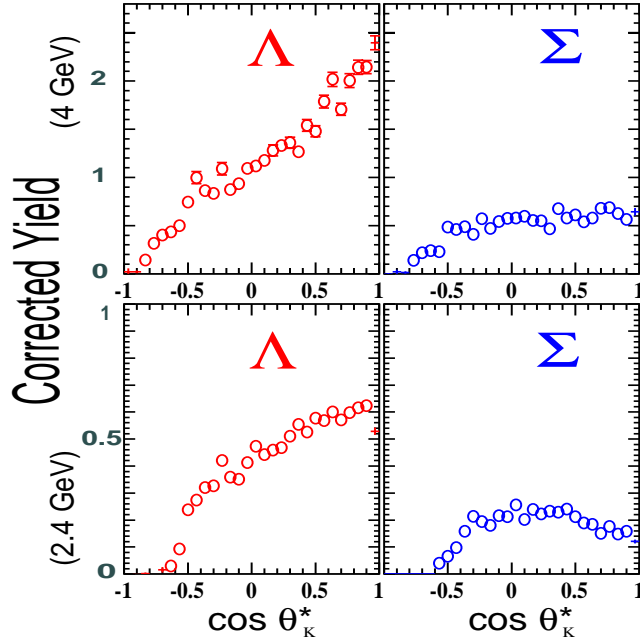


Figure 22: Preliminary CLAS data for hyperon production showing corrected yields for both  $\Lambda$  and  $\Sigma^0$  production as a function of  $\cos \theta_K^*$  for beam energies of 2.4 GeV (60% field) and 4.0 GeV (87% field).

## 4.2 $N^* \rightarrow KY$ Physics

The constituent-quark model provides a reasonable description of the static properties of the known hadrons. This is quite surprising since it is not clear how QCD reduces to the quark model in the static limit. Any serious discrepancies between the quark-model predictions

and experiment may give us insight into aspects of QCD, and how it may eventually be solved in the non-perturbative regime.

Despite the successes of the quark models, serious disagreements between their predictions and the known baryon spectrum have existed for some time. This gives rise to questions about the basic nature of excited-nucleon resonances. Are there baryons beyond the  $|qqq\rangle$  states? It is expected that  $|qqqq\rangle$  states should be copious, and some resonances may be “molecules” of the sort  $|qqq(\bar{q}q)\rangle$  [26]. Finding evidence of these states is important to clarify the intrinsic quark-gluon structure of baryons and the role played by the glue and mesons in hadron spectroscopy and structure.

Based on recent quark-model calculations, a large number of non-strange baryons appear to be missing. One early explanation to this dilemma involved the notion that pairs of quarks bind tightly into “diquarks” with a particular set of quantum numbers [27]. Baryons are then considered as quark-diquark systems, and the resulting symmetry qualitatively accounts for the missing states. Recent lattice QCD calculations seem to discredit this explanation [28].

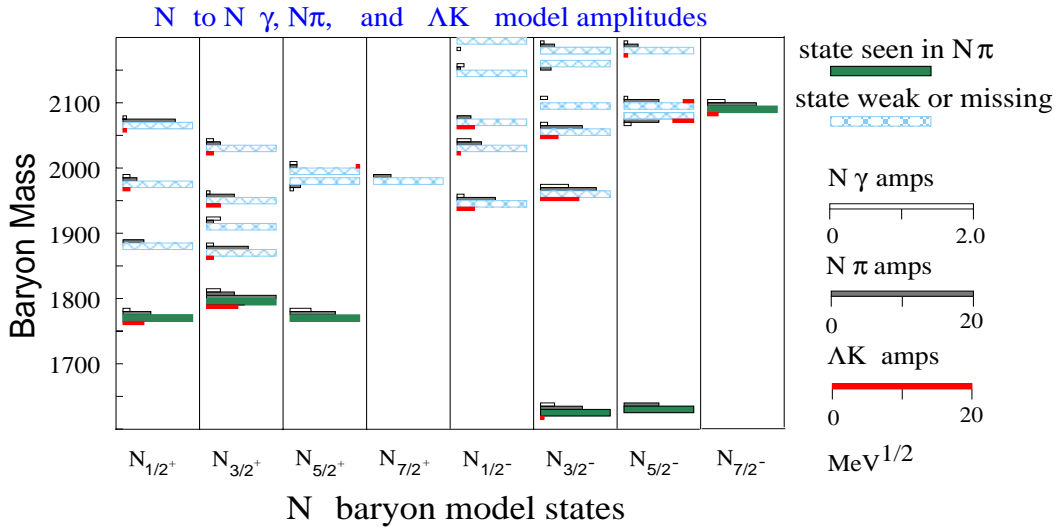


Figure 23: Mass predictions for decays  $N^* \rightarrow N\gamma, N\pi, \Lambda K$  for  $m \leq 2.2 \text{ GeV}/c^2$  [11]. States with significant amplitudes for  $N\gamma$  and  $\Lambda K$  decays should contribute strongly to the process  $\gamma N \rightarrow K\Lambda$ .

A less dramatic solution has also been suggested that appears to have some agreement with experiment. Nearly all data on the non-strange baryon spectrum consists of experiments with  $N\pi$  in the initial and/or final state. If the missing baryons do not couple strongly to  $N\pi$ , their signature may be extremely difficult to pull out from the data. Similarly, if the resonances are broad and overlapping, signals from weaker resonances will be overwhelmed by the stronger resonances. However, if there is a significant strength for decays of these  $N^*$  resonances to the  $K\Lambda$  or  $K\Sigma$  channels, they may become accessible through a reduction in the density of states.

This hypothesis is strongly supported by dynamical-quark calculations. Fig. 23 shows the mass predictions of one recent quark model for negative-parity non-strange baryons, whose wavefunctions lie predominantly in the  $N=3$  harmonic oscillator band, excited through the  $\gamma N \rightarrow K\Lambda$  reaction [11]. The figure shows that the amplitudes for decays into strange final states are generally smaller than those into the non-strange final states. However, in many

cases, only a few nearby states contribute with appreciable amplitudes, and the density of states that decay to strange final states is small. This is due in part to the higher thresholds in effect that allow these channels to turn on in the mass region where new states are predicted to be present. This is to be contrasted with the situation with non-strange final states where low-lying states with large amplitudes make extraction of information about higher-mass states with small amplitudes problematic.

The notion that decays of non-strange baryon resonances into strange final states should be present with a sizeable experimental signature has been backed up by recently published photoproduction data from SAPHIR [8]. These data have shown strong evidence through an angular decomposition of the differential cross section into Legendre polynomials that suggests the presence of  $N^*$  resonance production with decays to the  $K\Lambda$  final state at  $W = 1.72$  GeV. This could be due to resonance decay of the  $S_{11}(1650)$  and  $P_{11}(1710)$ , both of which couple to the  $K\Lambda$  channel.

Another method to be used to search for resonances is the comparison of the data with the standard hydrodynamic models. In such models, the input parameters in the calculations can be varied until good agreement is obtained with the data. While this method does not provide clear proof of the values of the coupling constants and resonance parameters, it can provide a guide to more in-depth theoretical studies. The recent kaon photoproduction data from SAPHIR, with a much higher statistical accuracy than previous data, has been analyzed in this way. The experimental data can be explained if the  $D_{13}(1960)$  resonance plays a significant role [7]. Now it is up to the quark models to explain why this resonance couples strongly in the kaon photoproduction channel.

This experiment at 6 GeV will allow us to probe baryon masses from the  $K\Lambda$  reaction threshold up to 3.0 GeV. Analysis of these data will yield information about the coupling of these resonances to final states involving excited strange baryons and mesons. Due to the difficulties of the separation of non-resonant background, unpolarized measurements are valuably complemented by polarization measurements. In fact the partial wave analyses that are required to extract the masses and spins of the baryonic resonances cannot be done in any meaningful way without polarization observables. Strangeness production could open up a new window for light quark baryon spectroscopy not available in the past.

A partial wave analysis of our final spectra will ultimately be required to extract spin-parity and decay widths of the  $s$ -channel baryonic resonances produced in the interaction. In this procedure we will attempt to parameterize the observed angular distributions in terms of resonance production amplitudes that span the appropriate space. Note that polarization measurements using CLAS have a greater advantage over other electromagnetic exclusive measurements in partial wave analyses. The capability of full  $4\pi$  angular acceptance and additional observables from polarization measurements make a less model-dependent partial wave analysis possible.

Recently, the Baryon Resonance Analysis Group (BRAG) has been formed with the specific intention of maintaining and overseeing the world data base, as well as directing systematic global fits to these data. One of the important tasks this group is undertaking is to better understand how to separate the effects of the resonant and non-resonant contributions to the different reaction channels. Our group intends to work closely with BRAG when the analysis has reached a sufficiently advanced stage.

## 5 Theoretical Approaches

There are a number of distinct theoretical approaches used to describe electromagnetic interactions. As introduced in Section 1, the three major descriptions include hadrodynamical models, quark models, and models based on Regge theory. The data from this proposal are expected to provide a unique opportunity for further development of each of these avenues. Furthermore, it is expected that detailed comparisons of these models to the observables of electroproduction, beyond allowing for improvements to the theories, will help to quantify the transition from non-perturbative to perturbative QCD. In the remainder of this section, further details regarding each of the three theories are described in specific relation to the data that will be acquired at 6 GeV.

### 5.1 Hadrodynamical Models

The main phenomenological method used in the investigation of the electromagnetic production of kaons is based on diagrammatic techniques through isobaric models [4, 5, 6]. In this approach, an effective Lagrangian is constructed by summing the Born terms and the contributions from the excitation of intermediate resonant states known as the extended Born terms in the  $s$ ,  $t$ , and  $u$  reaction channels shown in Fig. 24. The fact that both the incident photon and the outgoing kaon interact rather weakly with hadrons justifies the attempts to describe the process through models limited to first-order terms. First-order perturbation theory is employed to construct the scattering amplitude from the sum of diagrams corresponding to the exchange of one particle or resonance (tree approximation) in the intermediate state.

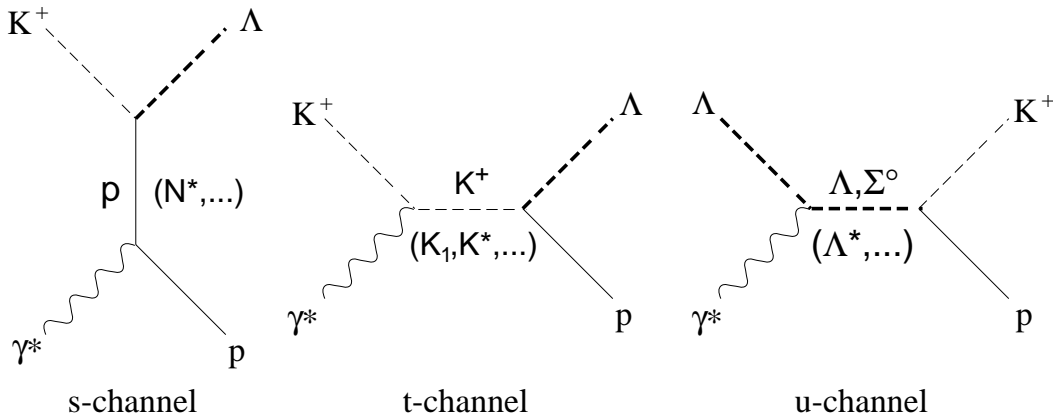


Figure 24: Resonance picture Feynman diagrams for the process  $\gamma^* p \rightarrow K^+ \Lambda$  for  $s$ ,  $t$ , and  $u$  channel reactions. The non-Born terms are listed within the parentheses.

These models were developed mostly from fits to experimental data by allowing for a limited number of intermediate resonances and leaving their coupling constants as free parameters. However, the limited data base permits only qualitative conclusions. For further development of these models, more cross section and polarization data is important to better understand which are the appropriate resonances to include in the intermediate state. The  $s$ ,  $t$ , and  $u$  reaction channels each contribute to the process in varying degrees depending

on the reaction kinematics, and each may go through a sizeable number of intermediate hadronic resonances. The presence of all these possible production mechanisms means that reliable hadrodynamical models require many parameters, and thus many observables over a broad kinematic range to constrain them.

There have been two important recent breakthroughs regarding the hadrodynamical model calculations for photoproduction that have strengthened the state of the existing calculations. The first is a recent coupled-channels analysis that has included hadronic rescattering for the first time [29]. The second advancement demonstrates how hadronic form factors can be included in a consistent and gauge invariant fashion. This provides the possibility of achieving good fits to the data with a  $K\Lambda N$  coupling constant close to SU(3) values [30]. Both advancements are being extended to electroproduction for both the  $K\Lambda N$  and  $K\Sigma N$  channels. Results including hadronic rescattering are expected in the near future. Currently available calculations including gauge invariant hadronic form factors are included in our polarization calculations shown in Figs. 9 and 10.

These phenomenological calculations are still limited by a sparsity of data, but the broad range of cross section and polarization measurements proposed at Jefferson Lab with energies up to 4 GeV should provide a wealth of data to strengthen and extend these models. One of the key aspects of these studies is a better determination as to which are the most important resonances to include in the intermediate states as well as their appropriate coupling constants. The best existing models include  $s$ -channel resonances up to and including spin 5/2. To maximize the range of validity of these models, the present calculations are attempting to include higher-spin  $u$ -channel resonances. These higher-spin resonances are expected to contribute to a much greater extent as the energy available in the intermediate state increases. Thus, due to the increased kinematical phase-space coverage, the push to 6 GeV should allow study over the full extent of the resonance region. With sufficient statistics to bin the data narrowly in  $Q^2$  and  $W$ , the calculations can be pushed to their limits. By taking advantage of the broad range of kinematics accessible with CLAS at 6 GeV, the failures of the models to explain the cross-section and polarization data can be fully exposed. Only then will the effects of the model deficiencies come to light.

## 5.2 Regge-Exchange Models

Data for the reaction  $\gamma^{(*)}p \rightarrow \pi N$  have been compared with a new model based on a Regge description [16]. At intermediate energies ( $E_\gamma \geq 2$  GeV) and momentum transfers ( $-t \leq 3$  (GeV/c)<sup>2</sup>), this Regge trajectory exchange model has proven to be superior to Born-diagram models when compared to the available published cross section and asymmetry data. The model has recently been extended to study  $K^+\Lambda$  and  $K^+\Sigma^0$  electroproduction in these same kinematics with coupling constants determined from kaon photoproduction reactions [17]. This gauge-invariant model provides a good description of the available unpolarized and polarized photoproduction data. Fig. 25 shows the results for the  $Q^2$  dependence of the  $\gamma^*p \rightarrow K^+\Lambda, \Sigma^0$  differential cross sections at  $\theta_K^*=8^\circ$  for two  $W$  bins. Calculations of the  $\Lambda$  polarization at 6 GeV are shown in Fig. 26 as a function of  $\cos \theta_K^*$ . The polarization components in the  $\vec{e}p \rightarrow e'K^+\vec{\Lambda}$  reaction are plotted for  $W=2.2$  GeV and fixed  $Q^2=1.0$  (GeV/c)<sup>2</sup> for the two fixed azimuthal angles  $\phi_K^* = 0^\circ, 180^\circ$ . In general, the predicted hyperon polarizations are much larger than those predicted by the hadrodynamical models.

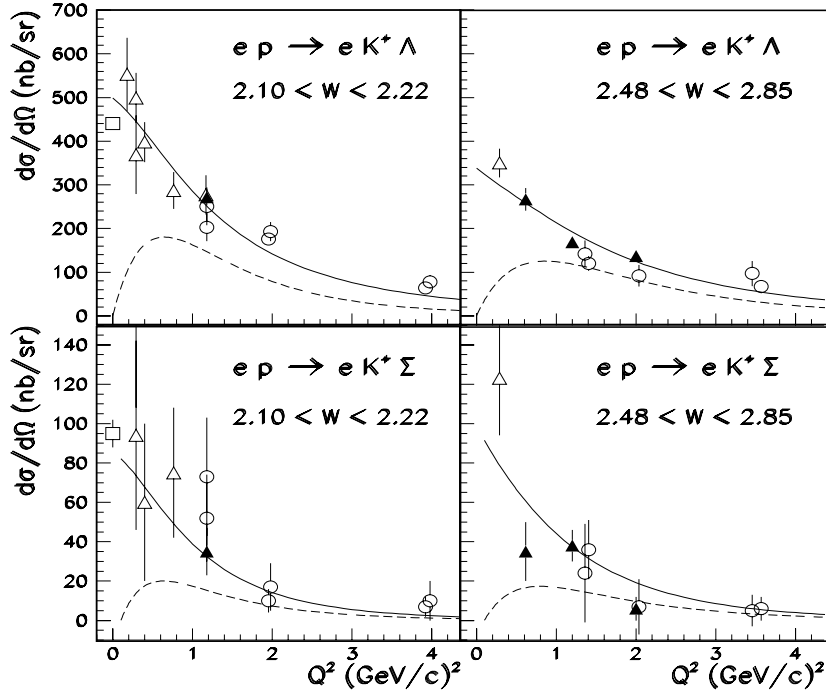


Figure 25:  $Q^2$  dependence of the  $\gamma^* p \rightarrow K^+ \Lambda, \Sigma^0$  differential cross sections for two energy bins. In the Regge calculations, the solid lines correspond to the summed  $L + T$  terms and the dashed line represents only  $\sigma_L$ . The displayed data correspond approximately to the same  $W$  and  $\theta_K^*$  ranges. See Ref. [16] for details on the calculations and the data points.

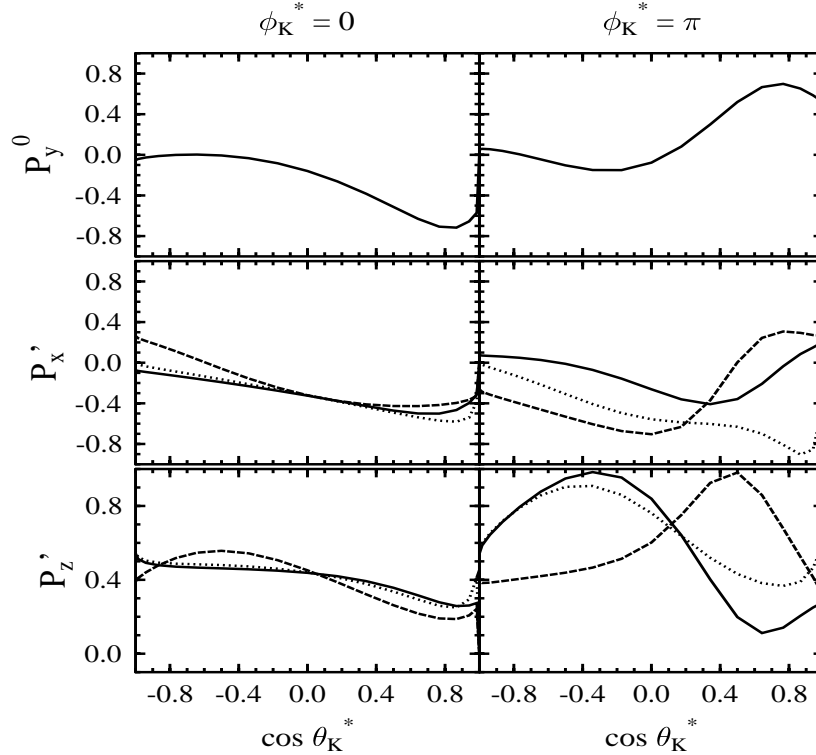


Figure 26: The  $\cos \theta_K^*$  dependence of the three  $\Lambda$  polarization components at 6 GeV for  $W=2.2$  GeV,  $Q^2=1.0$   $(\text{GeV}/c)^2$ , and for  $\phi_K^*=0, \pi$  from Regge-exchange calculations [16]. The solid curves are for the full calculation, the dashed curves are for  $K$  exchange only, and the dotted curves are for  $K^*$  exchange only.

Starting from a standard Feynman diagram formalism, the exchange of a Regge trajectory is accomplished by replacing the usual pole-like Feynman propagator of a single particle (i.e.  $1/(t - m^2)$ , where  $m$  is the mass of the exchanged particle) by a so-called Regge propagator. The Regge propagator represents a family of particles all with the same internal quantum numbers. The model is simple in that it is based on the  $K$  and  $K^*$  Regge exchanges in the  $t$ -channel.  $s$ -channel Born diagrams are included to preserve gauge invariance. In previous Regge models the cross sections were predicted only after inclusion of non-physical “over-absorption” terms [31], however, the current model reproduces both unpolarized and polarized observables over the full energy range of the existing data.

It is expected that detailed comparisons of this model to the observables of electroproduction (cross sections and polarization observables) will help to quantify the transition from the nonperturbative to perturbative QCD (pQCD) regimes. An extrapolation of the Regge model to momentum transfers where pQCD is valid has been performed for the pion photoproduction reaction with good results [17]. Similar extrapolations are planned for the kaon photo- and electroproduction reactions [32]. Data at these kinematics are particularly sparse. Therefore, measurements of kaon electroproduction observables above the resonance region are necessary for the development of theoretical models that bridge the transition region.

At lower energies, only enough energy is available in the intermediate state to create  $K$  and  $K^*$  resonances. To fully test the idea of Regge trajectory exchange, higher energies are necessary to create the higher-mass kaons in the intermediate state (the production probability of the higher-mass kaons is weighted essentially by the  $1/(t - m^2)$  propagator). Only through this study with beam energies up to 6 GeV can the notion of a trajectory exchange be more rigorously tested.

## 5.3 Quark Models

### 5.3.1 Quark-Pair Creation

Hadrodynamical calculations are expected to become increasingly deficient as the energy in the intermediate state moves beyond the limits of the resonance region. This occurs as quark and gluon degrees of freedom begin to dominate the reaction mechanism and hadronic degrees of freedom become less important. The hadrodynamical models are essentially based upon the assumption that the incident photon interacts with the nucleon as a whole, which is only valid at long incident photon wavelengths ( $\sim 1.0$  fm). At 6 GeV the wavelength is 0.2 fm and the photon can be considered to interact with the constituent quarks and gluons. Understanding the boundary between these two pictures is one of the key reasons for extending the measurement program to higher energies.

With the broad kinematic coverage of CLAS, there are a number of different quark-level diagrams for  $KY$  electroproduction that need to be considered, several of which are shown in Fig. 27. It is expected that these different contributions can be most effectively isolated by studying both cross sections and polarization observables as a function of  $Q^2$ ,  $W$ , and  $t$ .

The extension of the electroproduction measurements to 6 GeV may shed further light on strange quark production mechanisms. In one naive kaon electroproduction scenario, shown in Fig. 28, a polarized incident virtual photon interacts with one of the two  $u$  quarks of the

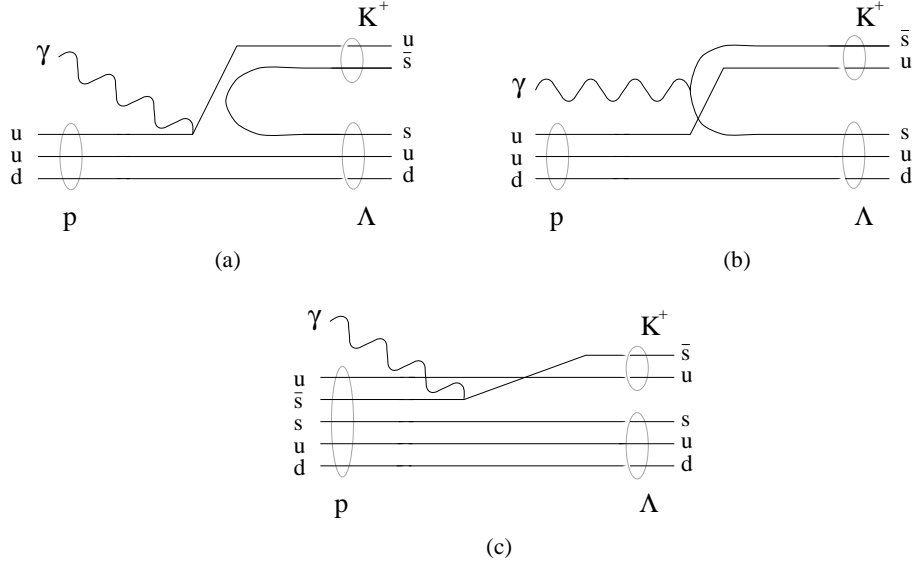


Figure 27: Some of the possible quark-flow diagrams for  $K\Lambda$  production. (a).  $s$ -channel Born diagram, (b). VMD diagram, (c). direct knockout of anti-strange quark.

target proton. This process is nearly an order of magnitude more likely than an interaction with the  $d$  quark. As the now polarized  $u$  quark recoils against the correlated  $u - d$  pair, a color string is believed to stretch between the recoiling quark-diquark system of the decaying  $N^*$  resonance until it becomes energetically favorable to create an  $s\bar{s}$  pair. Since the  $K^+$  has spin 0, and hence cannot carry polarization, this forces the spin of the  $\bar{s}$  quark to be aligned opposite to that of the  $u$  quark. As the spin of the  $\Lambda$  is believed to be carried almost entirely by the  $s$  quark [33], measurement of the  $\Lambda$  polarization can be used to study the spin alignment of the created  $s\bar{s}$  pair.

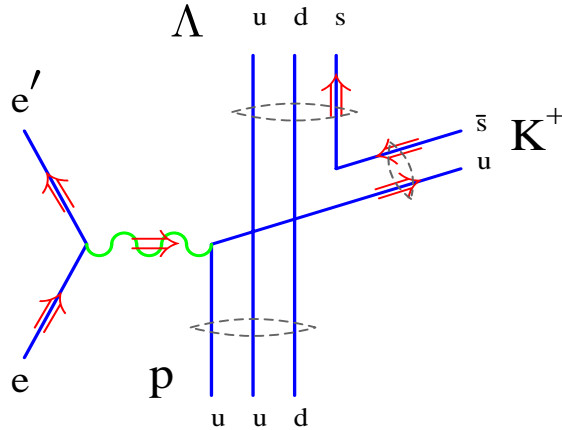


Figure 28: Quark-level diagram of the electroproduction of strangeness that is expected to become more valid as the energy of the virtual photon increases above the resonance region.

Strong decays of the type  $N^* \rightarrow KY$  are still a rather poorly understood area of hadronic physics. Calculations for this type of coupling are essential to understand the role of strangeness in the standard model, as well as the inter-quark potential. There have been

many attempts over the past 30 years to model strong decays through  $q\bar{q}$  pair production [11, 12, 13]. However, there is still a fair amount of ambiguity regarding the wavefunction of the  $q\bar{q}$  pair created. There have been suggestions that the quark pair should be created with vacuum quantum numbers [13], as well as suggestions that the pair should have quantum numbers of a single gluon [34]. Vacuum quantum numbers correspond to  $J^\pi=0^+$ . Since this corresponds to a  ${}^3P_0$   $q\bar{q}$  state, it is generally referred to as the  ${}^3P_0$  quark-pair creation model. Similarly the single gluon quantum numbers of  $J^\pi=1^-$  correspond to a  ${}^3S_1$   $q\bar{q}$  state. The  ${}^3S_1$  quark-pair creation model assumes that the  $q\bar{q}$  pair came from a single gluon (OGE). Regardless of the quantum numbers of the created quark pair, the fundamental decay mechanism is not understood.

At the present time the  ${}^3P_0$  model is more widely accepted than the  ${}^3S_1$  model due to its success for meson decay (especially the decays  $a_1 \rightarrow \omega\pi$ ,  $b_1 \rightarrow \omega\pi$ ). However, the  ${}^3P_0$  assumption fails in several cases such as the  $f_0 \rightarrow \pi\pi$  channel [12]. It is generally believed that both  ${}^3P_0$  and  ${}^3S_1$  mechanisms must be present but that  ${}^3P_0$  coupling is dominant [35]. Detailed tests of the decay models are therefore important and it is believed that polarization observables will provide for sensitive tests [11, 13]. The best tests of the decay models will come from final states that clearly result from a single intermediate  $N^*$  resonance. This is an important reason to select bins in  $W$  to be as narrow as possible (in order to isolate single resonances) or, alternatively, a careful partial wave analysis is required to pull out the resonant amplitudes with a given  $J^\pi$ .

Of course, understanding the process of kaon electroproduction through quark-pair creation should improve at 6 GeV as  $W$  increases beyond the resonance region. We then no longer have to worry about attempting to isolate single resonances in the intermediate state or combining data sets to accomplish partial wave analyses. With appropriate kinematic cuts we can essentially concentrate directly on a pure  $s$ -channel quark picture of the reaction as shown in Fig. 28.

### 5.3.2 Quark-Distribution Functions

The production of  $\Lambda$  hyperons in deep-inelastic scattering of leptons on the nucleon provides information on the quark content of the target nucleon [36]. It is also expected that these data may also provide information on the polarized-quark distributions and the quark-fragmentation functions [37]. These functions represent the probability of a quark fragmenting into a given hadron.

Experiments with polarized-electron beams on an unpolarized-proton target should provide information on the quark distributions and the quark-to- $\Lambda$  fragmentation functions [38]. These functions can supply information on the strange-quark content of the nucleon. In this regard, there have been recent pQCD calculations relating the  $\Lambda$  polarization to the underlying polarized-quark distributions, which in turn are related to the quark-fragmentation functions. These calculations have been compared with recent HERMES lepton deep-inelastic data for  $\Lambda$  spin transfer. The results are shown in Fig. 29 as a function of the variable  $z$  which represents the fractional  $\Lambda$  energy relative to the virtual photon. The two calculations shown are for the contributions of the valence and sea quarks. Also shown in Fig. 29 is the  $z$  range accessible to CLAS at 6 GeV, which is complementary to that covered by HERMES.

Comparisons of the data at 6 GeV to pQCD models will allow for further investigation

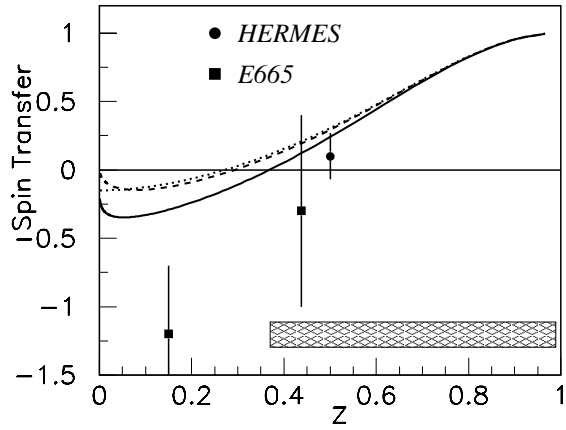


Figure 29: The  $z$ -dependence of the  $\Lambda$  spin transfer in electron deep-inelastic scattering. The dotted curve corresponds to pure valence-quark contributions and the solid curve to contributions from the quark sea. The horizontal band indicates the range of  $z$  accessible to CLAS at 6 GeV.

of the transition region and may bolster arguments for the evidence of quark-effect interpretations of the CLAS polarization data.

## 6 Performance of CLAS at 6 GeV

CLAS relies on precise time-of-flight (TOF) measurements and good momentum resolution to identify charged particles and to isolate exclusive channels using missing-mass techniques. These methods have been demonstrated to work well at energies up to 4 GeV. At higher energies, particle identification using TOF information alone will become more ambiguous, leading to larger backgrounds in our missing-mass distributions. The missing-mass resolution will also become increasingly poorer at the higher energies. New techniques will be required to achieve the desired experimental sensitivity.

In order to address these questions, a short test run was carried out in March 1999 with CLAS at a beam energy of 5.56 GeV, the highest energy available at CEBAF at that time. Data were taken with an electron trigger with a low-energy threshold for the calorimeter to provide the least-biased event selection. To maximize resolution, the torus magnetic field was at 90% of maximum. The results of this run show that the performance of CLAS at 5.56 GeV is sufficient to carry out the program described in this 6 GeV proposal.

To understand the performance of CLAS at 6 GeV, there are a number of important issues that must be considered. This list includes:

1. Electron/pion separation
2. Charged-particle identification
3. Final-state hyperon identification

In the following sections we address these issues from study of the data accumulated during the 5.56 GeV test run.

### 6.1 Electron/Pion Separation

Electron identification in CLAS relies on the combination of a signal from the Čerenkov detectors (sensitive to particles with  $\beta \geq 0.998$ ), and the energy deposition in the calorimeters matching the momentum as determined by the drift chambers. This technique is fully efficient for electron momenta below 2.7 GeV/c, but the Čerenkov counters start becoming efficient for pions above this limit. This background effect is somewhat offset, however, as the calorimeter resolution improves as  $1/\sqrt{E_{cal}}$  with increasing energy of the incident particles. Thus we will be able to impose tighter cuts for the candidate electrons at 6 GeV, improving our signal to background.

Fig. 30 shows the electron acceptance from the 5.56 GeV high-field CLAS data in terms of scattering angle versus momentum. A clear signature of the elastic scattering events is visible at the highest reconstructed electron momenta indicating that the pion background is not a major issue above 3 GeV/c. This analysis has employed very loose cuts on the calorimeter energy. At the lowest  $Q^2$  points we can also employ constrained kinematic fits to isolate our final states of interest.

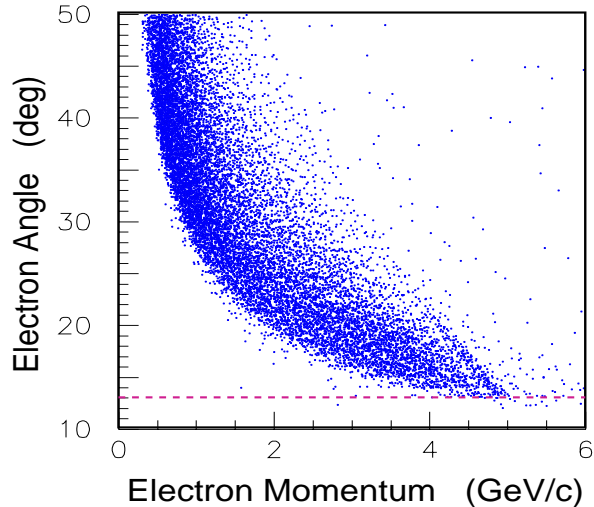


Figure 30: Electron angle versus momentum from 5.56 GeV high-field CLAS data. The minimum electron angle subtended by CLAS is about  $13^\circ$ .

## 6.2 Charged-Particle Identification

Charged hadrons ( $\pi$ ,  $K$ ,  $p$ ) are identified from their reconstructed mass by combining TOF information with momentum information from the drift chambers. They must traverse all three Regions of the drift chambers and strike the outer scintillation counters in order to be identified. Those with low momentum are curled up by the magnetic field and fail to reach the scintillators, while those with too small a production angle go down the forward hole between the coils of the torus magnet. Fig. 31 shows the mass spectrum of hadrons created in the  $ep \rightarrow e'X$  reaction at 5.56 GeV. A momentum-dependent cut on this spectrum is typically used to select the scattered hadrons during event reconstruction. The ratio of the pion and proton peaks to the kaon peak in this spectrum is quantitatively the same as for the corresponding 4 GeV spectrum.

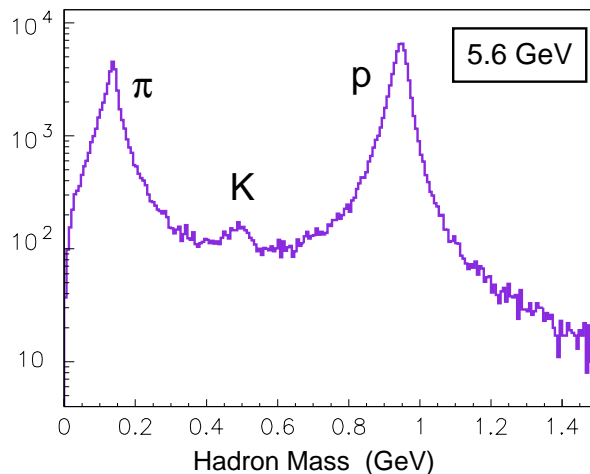


Figure 31: Hadron-mass distribution for positively charged particles produced at 5.56 GeV in  $ep \rightarrow e'X$ .

The quality of the charged-particle separation as a function of the momentum and velocity

of the particles is shown in Fig. 32. From this figure, the  $\pi$ ,  $K$ , and  $p$  bands are all clearly visible. This data sample includes a loose kaon-mass cut that enhances this band relative to the others. The highest momentum hadrons are going forward in the lab where the flight path to the scintillators is about 5 m. For small angles, the expected timing resolution of the scintillators is about 120 ps. With the current CLAS timing resolution and particle identification techniques,  $\pi$ ,  $K$ , and  $p$  can be distinguished up to  $\approx 2$  GeV/c. With this stated, it is important to note that at 6 GeV, kaon production proceeds in a kinematic regime where momenta remain relatively low. Furthermore, the kaons of interest for the  $L/T$  separation measurements at 6 GeV will be restricted to lower momenta since we have to match the  $Q^2$ ,  $W$ , and  $t$  ranges of the lower-energy data for these fits.

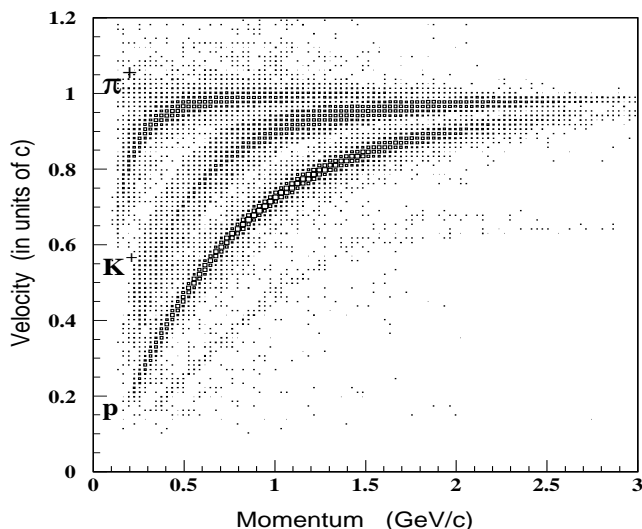


Figure 32: Charged-particle velocity versus momentum showing the separation of the  $\pi$ ,  $K$ , and  $p$  bands. The data sample includes a loose cut on kaons that enhances their appearance.

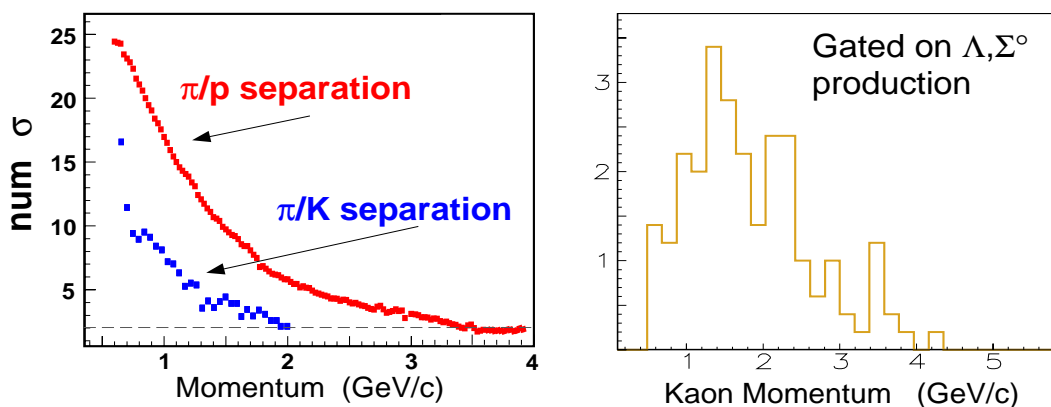


Figure 33: (a). Calculation of the separation (in  $\sigma$ ) between the calculated  $\pi/p$  and  $\pi/K$  flight times. (b). The momentum spectrum of kaons at 5.56 GeV associated with hyperon production.

Fig. 33a shows the expected separation between the different hadron bands as a function of the momentum. The separation is defined in terms of the difference between the calculated

flight times for the different particles using the expected timing resolution. It is expected that reasonable hadron separations can be achieved in the analysis down to a  $2\sigma$  separation.

Fig. 33b shows the momentum spectrum of the kaons associated with hyperon production at 5.56 GeV. Roughly 30% of the kaons associated with hyperon production have momenta above 2 GeV/c. From these data, the raw  $\pi/K$  ratio for momenta above 2 GeV/c is of order 10 to 20:1 without any cuts. Thus we do not believe that  $\pi/K$  separation in the high momentum region will be a major issue. However, if necessary, we could split the analysis into two regimes about 2 GeV/c. For  $p_K < 2$  GeV/c, we could require only the electron and kaon in the final state. For  $p_K > 2$  GeV/c, we could require the hyperon decay proton or pion as well. Requiring this additional particle greatly improves the hyperon signal as shown in Section 6.3.

An additional requirement that can be imposed to clean up our hyperon spectra is to require the decay proton to originate outside the target region. This reconstruction can already be handled with our current tracking algorithms. We also can employ constrained kinematic fits to improve separation of the  $KY$  final states from  $\pi N$  final states.

At the present time our analysis technique to reduce the background due to misidentified pions is to assign the kaon mass to all positive hadrons below the proton mass peak. If the positive hadron was indeed a kaon, then the final-state hyperon will be correctly reconstructed. If the positive hadron was a pion, it will then contribute to the underlying background. This can be subtracted by sorting a hyperon-mass spectrum gated by a known pure pion sample assigned the kaon mass. This technique was used to generate the background-subtracted recoil-mass spectrum for the 4 GeV data shown in Fig. 18. The contributing spectra used are shown in Fig. 34. The solid curve represents the recoil-mass distribution assuming all reconstructed hadrons in the mass range  $0.3 \leq m_h \leq 0.7$  GeV/c<sup>2</sup> were kaons. The dashed curve shows the normalized spectrum of good pions assigned the kaon mass. This technique may have applicability at 6 GeV as well if a pure final-state pion sample can be isolated.

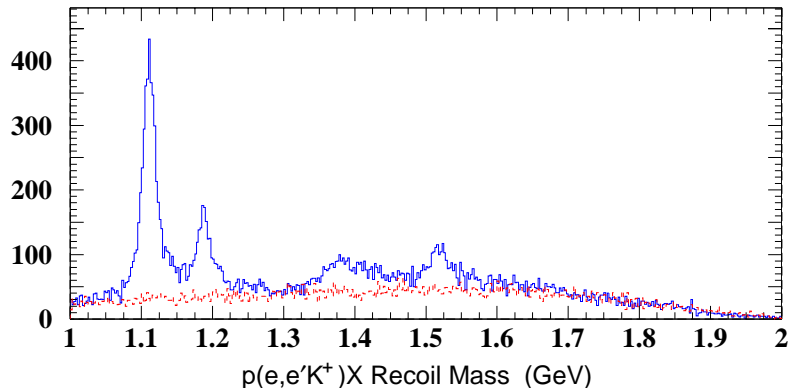


Figure 34: Recoil-mass spectrum for 4 GeV  $p(e, e'K^+)X$  CLAS data with all hadrons in the mass range from 0.3 - 0.7 GeV/c<sup>2</sup> assigned as kaons (solid line), and  $p(e, e'\pi^+)X$  with the pion assigned the kaon mass (dashed line). The background spectrum has been normalized to the portion of the hyperon spectrum below the  $\Lambda$  peak.

### 6.3 Final-State Hyperon Identification

The present CLAS program relies heavily on the missing-mass technique for the identification of neutral particles in exclusive reactions. Fig. 35 shows the present state of the hyperon reconstructions with the 4.247 and 5.56 GeV data sets. Shown in Fig. 35a are the missing-mass distributions for the  $ep \rightarrow e'K^+X$  CLAS data, cutting on the kaon peak in the hadron-mass spectrum. The main source of background beneath the hyperon peaks comes from pions misidentified as kaons, mainly from the reaction  $ep \rightarrow e'\pi^+\Delta^0$ . If the pion in this reaction is misidentified as a kaon, the resultant  $ep \rightarrow e'K^+X$  missing-mass distribution will have an overlapping contamination from this process. However, the 120 MeV width of the  $\Delta^0$  implies that this background will be much broader than the CLAS resolution-smeared hyperon missing-mass peaks. It has been found that the majority of these background pions can be eliminated with suitable cuts. Fig. 35c shows the final hyperon spectrum after cutting on the  $\pi^-$  peak in the  $ep \rightarrow e'K^+pX$  spectra shown in Fig. 35b. The width of the  $\Lambda$  peak from the 4.247 GeV data summed over all  $Q^2$  and  $W$  is about 14 MeV, while it is about 16 MeV for the q5.56 GeV data.

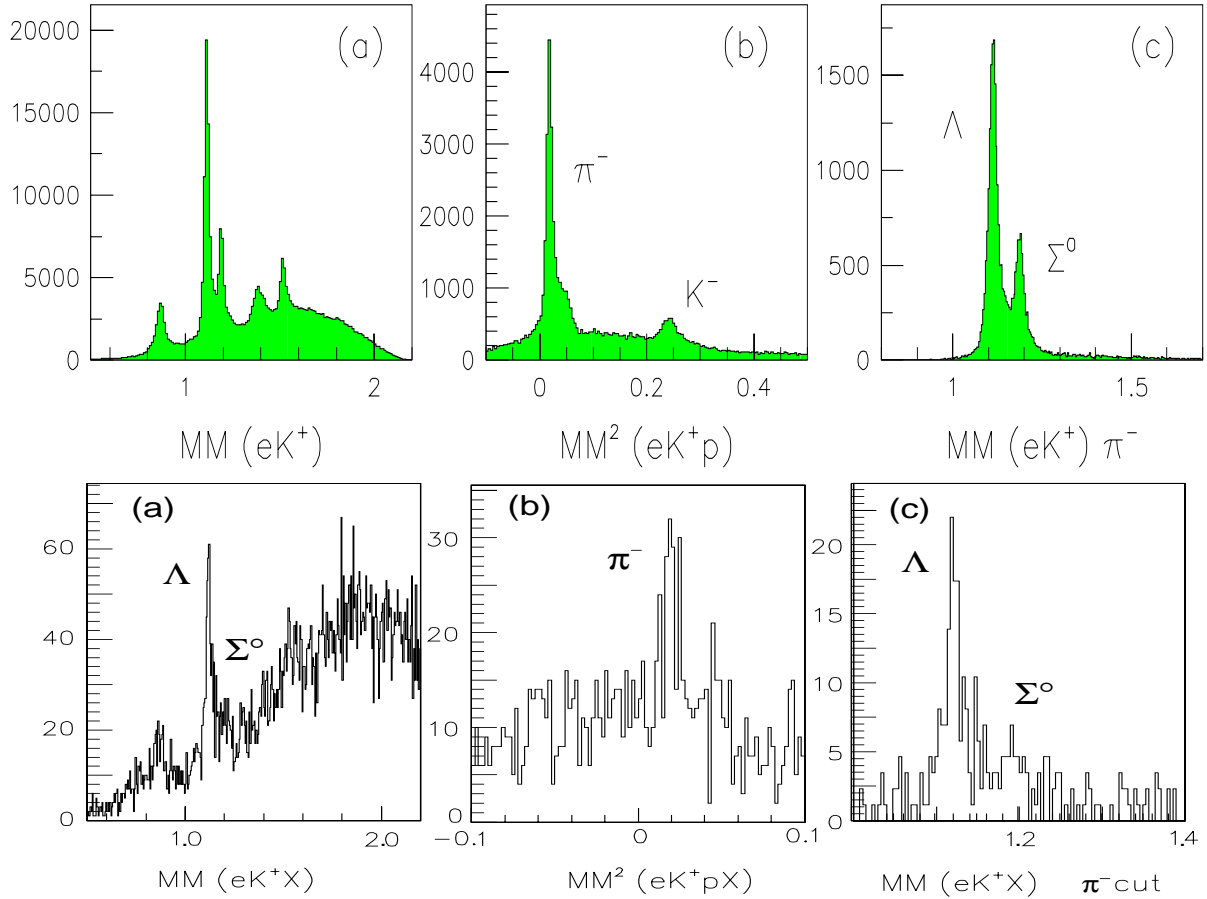


Figure 35: Missing-mass reconstructions for the  $\Lambda$  and  $\Sigma^0$  from 4.247 GeV (top) and 5.56 GeV (bottom) CLAS data. (a) The missing-mass spectra for  $p(e, e'K^+)X$ , (b) The missing  $\pi^-$  from the  $p(e, e'K^+p)X$  reaction, and (c) The hyperon distribution after cutting on the missing  $\pi^-$  peak.

## 7 CLAS Acceptance Function

In this section we present the results of our Monte Carlo study for this measurement. The Monte Carlo was written to help us better understand the kinematic and geometric acceptance of CLAS at 6 GeV. In our simulations, the  $ep \rightarrow e'K^+Y$  reaction was generated by weighting the event kinematics and angular distributions by the calculated cross section based on the WJC model [5]. At a given beam energy, four quantities are necessary to completely characterize the reaction in the laboratory system. These are  $W$ ,  $Q^2$ , and the CM angles of the kaon  $\theta_K^*$  and  $\phi_K^*$ . The input distributions are shown in Fig. 36. In addition, the reaction vertex position is also generated at the target.

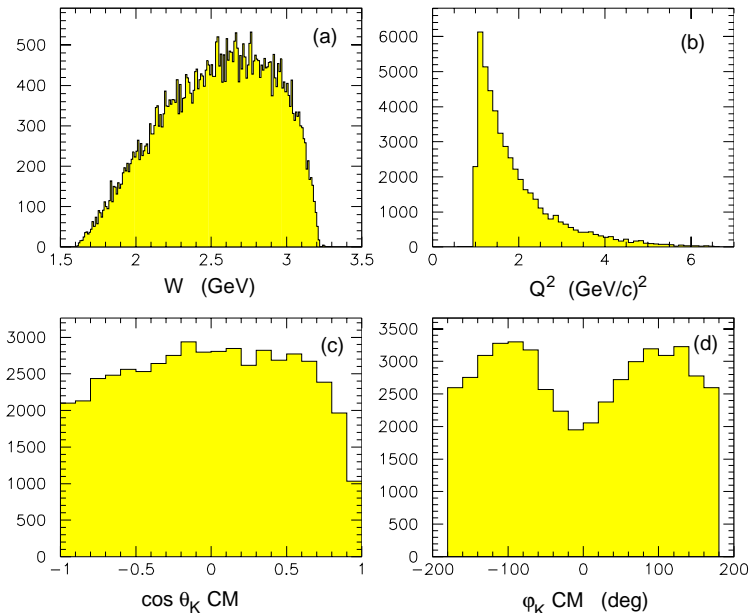


Figure 36: Kinematic distributions from the event generator for 6 GeV incident electrons. (a)  $W$  (GeV), (b)  $Q^2$  ( $\text{GeV}/c)^2$ , (c)  $\cos \theta_K^*$ , and (d)  $\phi_K^*$  (deg).

Our simulations of CLAS properly included the known dead wires in the drift-chamber system, the known drift-chamber position resolution, and the known resolutions of the TOF scintillators and calorimeters. The simulations also accounted for in-flight K and  $\Lambda$  decays from their known life times. Radiative effects on the scattered electron were also modeled [39]. The momentum, angles, and position of each particle were reconstructed at the target using the standard CLAS analysis software packages. All simulations were performed at the maximum CLAS torus magnetic field.

The CLAS acceptance for the  $ep \rightarrow e'K^+X$  reaction, detecting only the scattered electron and electro-produced kaon is shown in Fig. 37 as a function of  $\cos \theta_K^*$ . The average acceptance of CLAS over all  $Q^2$  and  $W$  for the  $e'K^+$  two-body final state is roughly 20%.

In determining the CLAS acceptance function for the  $ep \rightarrow e'K^+p$  three-body final state, the momentum and angles of the  $\Lambda \rightarrow p + \pi^-$  and  $n + \pi^0$  decay branches were generated isotropically in the  $\Lambda$  rest frame. Our acceptance function accounts for the fact that we only reconstruct the charged-hadron decay branch of the  $\Lambda$  hyperons (B.R.=0.64). Fig. 38 shows the three-body CLAS acceptance at 6 GeV for the three spin-quantization axes averaging over all  $Q^2$  and  $W$ . In this scenario, the average CLAS acceptance is roughly 5%.

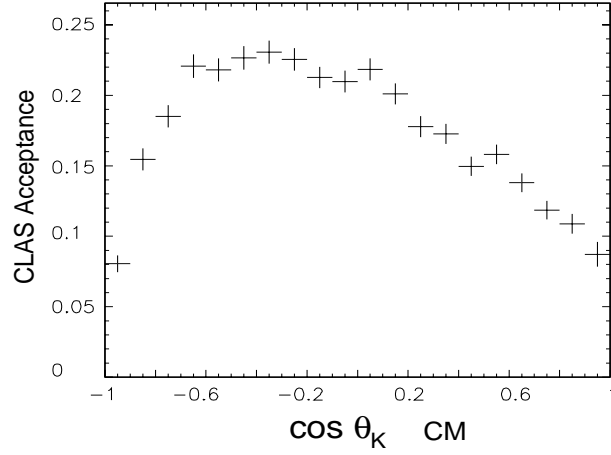


Figure 37: CLAS acceptance function for  $ep \rightarrow e'K^+\Lambda$  summed over all  $Q^2$  and  $W$  from 6 GeV Monte Carlo studies.

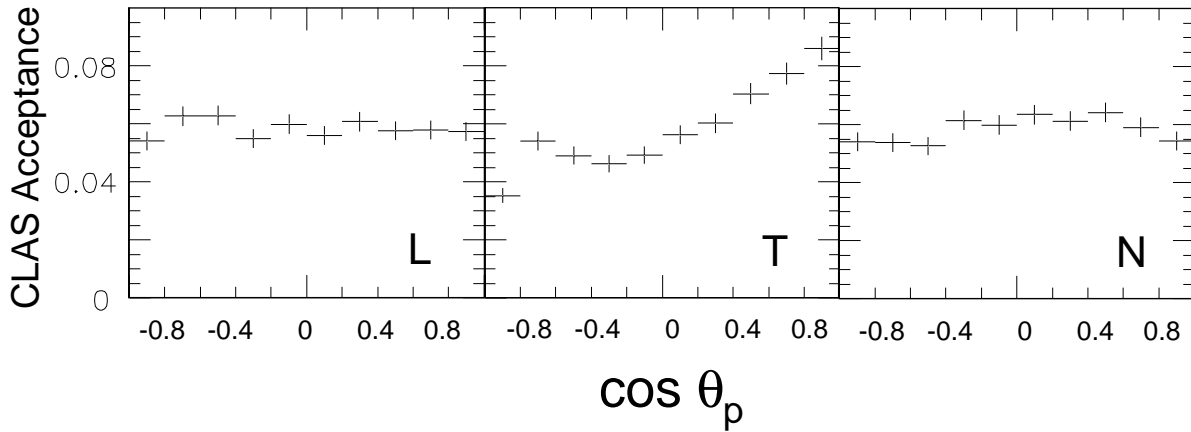


Figure 38: CLAS acceptance function for  $ep \rightarrow e'K^+pX$  as a function of  $\cos\theta_p^{RF}$  summed over all  $Q^2$  and  $W$  from 6 GeV Monte Carlo studies for the three different spin-polarization axes for the  $\Lambda$ .

## 8 Experimental Details

### 8.1 Data Binning and Statistical Precision

The 6 GeV data set will span a range of  $Q^2$  from 1.5 to 5 (GeV/c)<sup>2</sup> and  $W$  from 1.6 to 3.0 GeV. With this sizeable kinematic coverage, choice of our bin sizes is an important point. We have chosen 50 MeV wide bins in  $W$  as a compromise between our desire to isolate individual resonances and the limited statistics of the experiment. Also in keeping with the binning choices of E93-030 and E99-006, we have selected bins in  $Q^2$  of 0.5 (GeV/c)<sup>2</sup> for our estimates, although we will ultimately have to optimize the bin size choices once the full data set is in hand. The expected counting rate in each bin is given by:

$$RATE = \mathcal{L} \cdot \Gamma_v \cdot \sigma_v^{tot}(Q^2, W) \cdot \Delta Q^2 \cdot \Delta W \cdot ACC. \quad (12)$$

In this expression,  $\mathcal{L}$  is the beam-target luminosity,  $\Gamma_v$  is the virtual-photon flux factor,  $\sigma_v^{tot}(Q^2, W)$  is the total virtual-photon cross section integrated over all hadronic CM angles ( $d\Omega_K^*$ ),  $\Delta Q^2$  and  $\Delta W$  are our chosen bin sizes, and  $ACC$  is the CLAS acceptance for the final state of interest.

$W$	$Q^2$	$e'K^+$	$e'K^+p$	$W$	$Q^2$	$e'K^+$	$e'K^+p$
1.7	1.5	43460	10870	2.3	1.5	28990	7250
	2.0	12910	3230		2.0	11250	2810
	2.5	4510	1130		2.5	4810	1200
	3.0	1770	440		3.0	2200	550
	3.5	750	190		3.5	1050	260
	4.0	340	90		4.0	510	130
1.9	1.5	44690	11170	2.5	1.5	19660	4920
	2.0	14840	3710		2.0	7990	2000
	2.5	5640	1410		2.5	3520	880
	3.0	2360	590		3.0	1630	410
	3.5	1060	260		3.5	770	190
	4.0	500	120		4.0	370	90
2.1	1.5	38380	9600	2.7	1.5	11930	2980
	2.0	13930	3480		2.0	4940	1230
	2.5	5660	1420		2.5	2170	540
	3.0	2490	620		3.0	970	240
	3.5	1160	290		3.5	430	110
	4.0	560	140		4.0	170	40

Table 3: Expected counts at 6 GeV for representative bins in  $Q^2/W$  bins for a 60 day run at a luminosity of  $5 \times 10^{33} \text{ cm}^{-2}\text{s}^{-1}$ . A simple quark model has been used to extrapolate from the existing electroproduction cross-section data. Energies and momenta in GeV.

To estimate the counting rates for this proposal we have employed a simple quark model which reasonably accounts for the expected  $Q^2$  and  $W$  dependence of the cross sections.

Our calculated total cross sections were then scaled by a factor to constrain the rates over all  $Q^2/W$  to agree with the rates measured in CLAS at 5.56 GeV. This full procedure is described in Appendix Section 10.4.

For the differential cross-section measurements, we have determined how long we need to run to achieve a 3% statistical error over our  $Q^2/W$  bins allowing for 10 bins in  $\theta_K^*/\phi_K^*$ . To achieve a 3% error on average requires a total of about 12000 counts per bin, or about 1400 hours of running at a single torus magnetic-field setting. Table 3 reports our expected  $e'K^+$  yields for a 60 day run for representative  $Q^2/W$  bins at a luminosity of  $5 \times 10^{33} \text{ cm}^{-2}\text{s}^{-1}$ .

Table 3 also allows us to estimate the statistical precision of our  $\Lambda$  polarization measurements. Each polarization component and its associated statistical error can be defined as:

$$P_\Lambda = \frac{2}{\eta\alpha} \cdot \frac{N_+ - N_-}{N_+ + N_-}, \quad \sigma_{P_\Lambda} = \frac{2}{\alpha\eta\sqrt{N_0}} \cdot \left(1 - \frac{1}{4}\alpha^2 P_\Lambda^2\right)^{1/2}. \quad (13)$$

In this expression,  $\eta$  is the electron-beam polarization and  $\alpha$  is the  $\Lambda$  weak-decay asymmetry parameter. The total number of  $\Lambda$  decay protons detected in each  $Q^2$ ,  $W$ , and  $d\Omega_K^*$  bin is  $N_0 = N_+ + N_-$ . The number of protons in the  $\Lambda$  rest frame going forward and backwards (relative to the coordinate being considered) is given by  $N_+$  and  $N_-$ , respectively. Eq(13) also makes it clear that the *highest* possible beam polarization is important to reduce our measurement uncertainties.

At the present time, the e1 run group is scheduled for 30 days of 6 GeV beam time in 2001. From the standpoint of statistical uncertainties alone, a run of this limited duration will not allow for high-quality hyperon-polarization measurements in the narrow  $W$  bins we deem essential for this program. A total run duration of 60 days will allow for statistically meaningful polarization measurements over the  $W$  range up to 3.0 GeV in the narrow bins required.

	Absolute Statistical Uncertainty						
$Q^2 \downarrow \setminus W \rightarrow$	1.7	1.9	2.1	2.3	2.5	2.7	2.9
1.5	$\pm 0.09$	$\pm 0.08$	$\pm 0.09$	$\pm 0.11$	$\pm 0.13$	$\pm 0.16$	$\pm 0.23$
2.0	$\pm 0.16$	$\pm 0.15$	$\pm 0.15$	$\pm 0.17$	$\pm 0.20$	$\pm 0.25$	$\pm 0.36$
2.5	$\pm 0.27$	$\pm 0.24$	$\pm 0.24$	$\pm 0.26$	$\pm 0.30$	$\pm 0.38$	$\pm 0.57$
$Q^2$ bins : 0.5 (GeV/c) <sup>2</sup> , $W$ bins : 0.05 GeV $d\Omega_p^{RF}$ bins = 1, $\cos \theta_K^*$ bins = 4, $\phi_K^*$ bins = 1							

Table 4: Expected absolute  $\Lambda$  polarization statistical uncertainties at 6 GeV for representative bins in  $Q^2/W$  for a 60 day run at a luminosity of  $5 \times 10^{33} \text{ cm}^{-2}\text{s}^{-1}$  and 70% electron-beam polarization for a given choice of binning in  $d\Omega_K^*$ .

Our expected absolute statistical uncertainties on the  $\Lambda$  polarization are shown in Table 4 for one binning choice in  $Q^2$ ,  $W$ ,  $\cos \theta_K^*$ , and  $\phi_K^*$ . In determining the statistical uncertainty for the polarization measurements, a beam polarization of 70% and a luminosity of  $5 \times 10^{33} \text{ cm}^{-2}\text{s}^{-1}$  have been assumed with a run duration totaling 60 days. The total predicted

production rate of  $\Lambda$  hyperons detected through the  $e'K^+p$  final state over all  $Q^2/W$  bins is 79/hour. Analysis of 5.56 GeV CLAS data shows this number to be  $76\pm 8$ /hour.

## 8.2 Cross-Section Systematics

Our two primary sources of systematic uncertainties include those associated with determination of the kinematic variables ( $Q^2$ ,  $W$ ,  $\cos\theta_K^*$ ,  $\phi_K^*$ , etc.) and those associated with conditions of the experimental apparatus. In this regard, for physically meaningful results on the structure functions and  $L/T$  ratio to be extracted from the data sets, it is important that both the point-to-point uncertainties and the overall scale of the cross-section measurements be well understood. Both sources of uncertainty have a direct influence on the quality of the data extracted, or in other words, our measurements of the absolute cross sections. To this end, this section describes our efforts in attempting to understand the expected level of both types of uncertainty and their expected influence on our measurements.

#	Source	Uncertainty (%)		Studies Employed
		<b>P-to-P</b>	<b>Scale</b>	
1	Beam Energy	0.3-0.7	-	Allow 1.e-3 change from “nominal” value.
2	Electron Mom.	<0.3	-	Allow 2.e-3 change from “nominal” value.
3	Electron Angle	0.5-1.4	-	Allow 1 mr change from “nominal” value.
4	Kaon Mom.	0.1-0.4	-	Allow 2.e-3 change from “nominal” value.
5	Kaon Angle	< 0.1	-	Allow 1 mr change from “nominal” value.
6	Background	1.0	4.0	RMS of yields. Counts below $\Lambda$ threshold.
7	Acceptance	5	5.0	Data vs GSIM. Spread of GSIM samples.
8	Efficiency e-	1.0	0.5	Eff. vs Rate. Variations run-to-run.
9	Efficiency K+	0.5	1.0	Eff. vs Rate. Variations run-to-run.
10	Live Time	0.2-0.3	-	Within a run, run-to-run. FC and Time info.
11	Decay	0.5	2.0	GSIM vs theoretical survival rates.
12	Target Density	0.3-0.5	0.7	P-T curve; equation of state.
13	Abs. Charge	0.5	5.0	Elastic Analysis. Variation in current.
14	Rad. Corr.	3	4.0	Data/GSIM comp. (in the tail). RC vs $\epsilon$
15	Empty Target	0.3	0.5	D <sub>2</sub> monitoring.
16	Binning Corr.	0.3	2.0	Study of model differences.
	<b>TOTAL</b>	6.2-6.5	$\sim 10$ .	

Table 5: Systematic uncertainties in the  $p(e, e'K^+)Y$  analysis. Error types (by column) : **P-to-P**: Random point-to-point; **Scale**: Scale-type effects.

In Table 5, a complete summary of all known sources of systematic uncertainty is provided. This table is followed by a slightly more detailed description of the entries and how they were determined. Only the uncertainties larger than 0.1% are listed. Point-to-point effects that are relevant for  $L/T$  separations are listed separately from the scale-type effects that are important for absolute cross-section measurements.

[1-5] - **Central kinematics:** Variation of the cross section due to the finite resolution in the central kinematics ( $Q^2$ ,  $W$ ,  $t$ , etc.). The estimate is based on allowing the values of the beam energy and the electron and kaon momenta and angles to vary about their nominal settings. The WJC model [5] was used to compute the expected value of the cross section for all possible combinations.

[6] - **Background Subtraction:** The uncertainty was based on the RMS variation of the hyperon yield obtained after the subtraction of smooth backgrounds in the  $(e, e'K^+)$  spectrum in each bin. For each bin four different functional forms for the background were considered.

[7] - **Acceptance:** The reconstructed Monte Carlo yield was compared with the background-subtracted yield from the data. Also the Monte Carlo events were split into several independent samples and the spread in acceptance was taken as a measure of the systematic uncertainty. Some details of the acceptance calculation are contained in Section 7. Our 5% point-to-point assigned value for the contribution is expected to be a conservative estimate.

[8-9] - **Electron and Kaon Identification:** The run-by-run variation of the electron and kaon yields (for runs taken in the same experimental conditions) was taken into account. Additionally, the particle-identification cuts (energy deposition in the calorimeter, TOF mass, etc.) were varied around their “nominal” settings and the spread in electron/kaon yield was taken as a measure of the systematic uncertainty.

[10] - **Live time:** Based on the recorded Faraday cup and scaler information.

[11] - **Decay Correction:** Based on the difference between the ratio of reconstructed/thrown kaon events and the expected survival probability (exponential decay law), evaluated for the average path length of kaons through the CLAS detector.

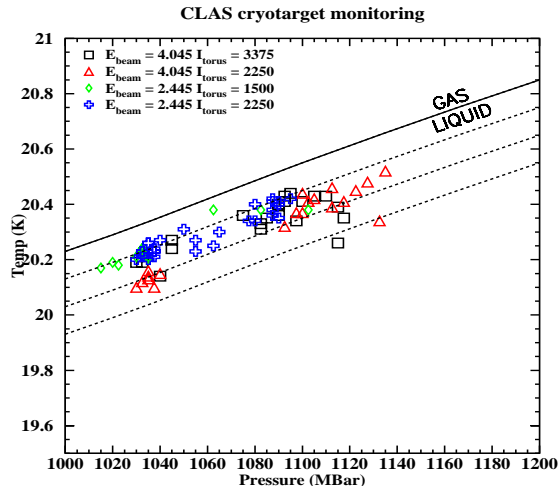


Figure 39: Target temperature and pressure measurements for various eI running conditions. The lines represent the theoretical p-T curve (solid) and curves corresponding to para-hydrogen liquids sub-cooled by 100, 200, and 300 mK, respectively.

[12] - **Target Density Fluctuations:** The fluctuations in the target density were monitored during production running with the temperature and pressure continuously recorded. In Fig. 39 these data are shown for various beam and CLAS torus conditions. The equation of state for liquid (para)hydrogen was used to evaluate the changes in density corresponding to the observed  $p$  and  $T$  fluctuations.

[13] - **Absolute Charge:** Our estimates were based on a comparison between the elastic electron scattering cross section as measured with CLAS and the world data set (see Appendix Section 10.3). The spread in the beam currents between different CLAS running conditions (i.e. beam energies) is also taken into account.

[14] - **Radiative Corrections:** The radiative correction prescription used in the present analysis is a variation of the procedure outlined in Ref.[39]. At the present time our cross-section model is based on an extended VMD theoretical model [40]. Our program uses the soft-photon approximation and the peaking approximation for the emitted photons. With these two assumptions, we compute  $\epsilon$  from the nominal kinematic values without any correction. Then for each bin we correct the measured cross section by a factor given by the ratio between the non-radiated and the radiated model cross sections. In Fig. 40 the  $Q^2$  and  $W$  dependence of the radiative correction factors is shown for beam energies of 4.247 GeV and 2.567 GeV. This figure shows that the radiative effects are of the order of 20-30%. The occasional upward swings are located towards the edges of the  $Q^2 - W$  space and correspond to bins where our coverage is incomplete. These bins will be rejected by subsequent fiducial cuts. Assuming that the model cross sections employed and the radiative correction prescription itself are good to  $\sim 10\%$ , one is left with an uncertainty of about 2-3% (or less) due to radiative corrections.

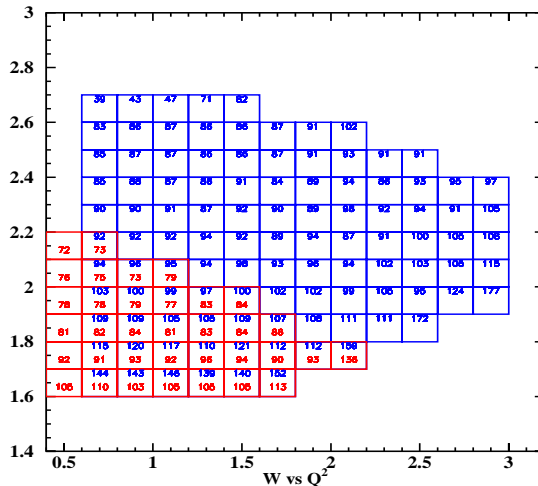


Figure 40:  $Q^2$  and  $W$  dependence of the radiative correction factors (in percent) for  $E_{beam} = 4.247$  GeV (upper numbers) and  $2.567$  GeV (lower numbers).

[15] - **Empty Target Subtraction:** Based on the effective target wall thickness as monitored by the deuteron yield.

[16] - **Bin Centering Correction:** As the binning of the data is rather coarse in some of the kinematic variables, there are systematic effects due to the non-linearity of the cross section within a bin. These were estimated from the difference between theoretical models within each bin.

### 8.3 Polarization Systematics

The effects of systematic uncertainties enter differently for the polarization components and the effects are also somewhat different for each component. Since we measure each polarization component integrated over  $\phi_K^*$ , there is no helicity-dependent component in  $P_y$ . In this situation it is not possible to extract the polarization component without knowledge of the CLAS acceptance function. On the other hand, there are no helicity-independent polarization components for  $P_x$  and  $P_z$ . In this case the CLAS acceptance function cancels out as discussed in Section 3.4. However, in this case, we have an uncertainty due to the electron-beam polarization.

Table 6 summarizes the sources and estimated individual systematic uncertainties for the three polarization components. The total is the sum of each of the individual sources of uncertainty added in quadrature. All estimates are preliminary and we are continuing our analysis to improve our understanding of the systematics.

Source of Uncertainty	$\sigma_{P_x}$	$\sigma_{P_y}$	$\sigma_{P_z}$
Beam Helicity	0.030	0.00	0.030
Proton Acceptance	0.00	0.04	0.00
Background ( $\Sigma^0$ , $\pi^+$ etc.)	0.03	0.03	0.03
Angle	0.015	0.015	0.015
Momentum	0.025	0.025	0.025
Beam Energy	0.010	0.010	0.010
Radiative Corrections	0.015	0.015	0.015
<b>Total</b>	$\pm 0.055$	$\pm 0.061$	$\pm 0.055$

Table 6: A list of the sources of absolute systematic uncertainty for each polarization component at 6 GeV.

Included in Table 6 is an entry for background contamination. As mentioned earlier, our hyperon missing-mass spectrum is contaminated mainly by the  $ep \rightarrow e'\pi^+\Delta^0$  reaction, where the pions are misidentified as kaons. This contribution is effectively removed with a cut on the  $\pi^-$  missing mass in the  $p(e, e'K^+p)$  reconstruction. The other important background reaction to consider is  $ep \rightarrow e'K^+\Sigma^0$ , where the  $\Sigma^0$  polarization dilutes the  $\Lambda$  polarization. Our cut on  $\Lambda$  missing mass will include a  $\sim 20\%$  contamination from  $\Sigma^0$ s due to the resolution of CLAS, which must be taken into account. Presently no electroproduction data exist for either the induced or transferred  $\Sigma^0$  polarization. However, these quantities for the  $\Sigma^0$  have been calculated for photoproduction [4]. These calculations show that the  $\Sigma^0$  polarization has comparable magnitude to the predicted  $\Lambda$  polarization, but is typically opposite in sign.

In the end we will also have a number of self-consistency checks with respect to the polarization observables that will help us to better understand our systematic uncertainties. This list includes: *(i)*. After integration over  $\phi_K^*$ , the polarization components  $P_x^0$ ,  $P_z^0$ , and  $P_y'$  must be zero. Deviations from zero will indicate problems with acceptance or energy calibrations. *(ii)*. We can also bin data on a CLAS sector-by-sector basis so that any sector dependencies can be determined and corrected. *(iii)*. The results for  $P_y^0$  must be independent of the helicity state of the electron beam.

## 9 Summary and Beam Time Request

This proposal describes a program to study exclusive kaon electroproduction with CLAS at 6 GeV using the  $ep \rightarrow e'K^+Y$  reaction. In part, this program represents an extension of the lower-energy strangeness production experiments E89-043, E93-030, and E99-006 currently included in the e1 run group in Hall B. The extension to a beam energy of 6 GeV will increase the available  $Q^2$  range from  $2.5 \text{ (GeV/c)}^2$  to  $5 \text{ (GeV/c)}^2$ , the available  $W$  range from 2.4 GeV to 3.0 GeV, and the available  $|t|$  range from  $3 \text{ (GeV/c)}^2$  to  $5 \text{ (GeV/c)}^2$  as compared to the coverage of the approved lower-energy program. These data are expected to provide a unique opportunity for the further development of the theoretical descriptions of open-strangeness production within and beyond the resonance region. The data acquired will allow for detailed tests of hadrodynamical models, constituent-quark models, and models based on Regge theory.

While these data are important for improving existing low-energy theoretical descriptions of the elementary strangeness-production process, the extension of strangeness production studies to higher-beam energies will also help to elucidate the transition from hadronic to quark-gluon degrees of freedom. This will allow for tests of the validity of non-perturbative QCD in these kinematics. Additionally, the higher-energy data will allow exploration of the wavefunction of the  $s\bar{s}$  quark pair created through the color flux-tube breaking in the intermediate state and possible access to the underlying quark-distribution functions of the proton.

At the present time detailed analysis of the lower-energy CLAS data is ongoing and the analysis is maturing at a rapid pace. All of the principals from the lower-energy measurements are involved in the proposed program. The analysis techniques, software, and experience that have been developed for analysis of the lower-energy data will be employed for analyzing the 6 GeV data.

This proposal requests 30 days of new beam time at 6 GeV. This new beam time, along with the 30 days already approved at 6 GeV and scheduled to run in 2001, are essential in order to measure the  $Q^2$ ,  $W$ , and  $t$  dependence of the hyperon cross sections and polarization over the narrowest bins possible for both  $\Lambda$  and  $\Sigma$  production. The experiment requires running with highly polarized electrons on the standard Hall B liquid hydrogen target with the CLAS spectrometer at maximum magnetic field. This experiment uses the standard CLAS electron-beam detector system, high-efficiency electron trigger, and data acquisition system.

## 10 Appendix

### 10.1 Response-Function Formalism

The kaon differential cross section, in the notation of Ref.[41], is given in terms of response functions  $R^{\beta\alpha}$  as:

$$\begin{aligned} \frac{d\sigma_v}{d\Omega_K^*} = & K_{CM} S_\alpha S_\beta \left[ R_T^{\beta\alpha} + \epsilon_L R_L^{\beta\alpha} + c_+ ({}^c R_{TL}^{\beta\alpha} \cos \phi_K^* + {}^s R_{TL}^{\beta\alpha} \sin \phi_K^*) \right. \\ & + \epsilon ({}^c R_{TT}^{\beta\alpha} \cos 2\phi_K^* + {}^s R_{TT}^{\beta\alpha} \sin 2\phi_K^*) \\ & \left. + hc_- ({}^c R_{TL'}^{\beta\alpha} \cos \phi_K^* + {}^s R_{TL'}^{\beta\alpha} \sin \phi_K^*) + hc_0 R_{TT'}^{\beta\alpha} \right]. \end{aligned} \quad (14)$$

The  $R^{\beta\alpha}$  factors are real or imaginary parts of bilinear combinations of the CGLN amplitudes for kaon electroproduction, and depend on the independent kinematic variables  $\theta_K^*$ ,  $Q^2$ , and  $W$ . In this expression,  $h$  is the electron beam helicity,  $\phi_K^*$  is the laboratory azimuthal angle of the outgoing kaon, and  $\epsilon$  ( $\epsilon_L$ ) is the transverse (longitudinal) component of the virtual photon polarization. The parameters  $c_\pm = \sqrt{2\epsilon_L(1 \pm \epsilon)}$  and  $c_0 = \sqrt{1 - \epsilon^2}$  represent kinematic factors, and  $K_{CM}$  is defined as the ratio of CM momentum of the  $\gamma^*$  relative to the  $K^+$ . In eq(14)  $S_\alpha = (1, \hat{S}_x, \hat{S}_y, \hat{S}_z)$  and  $S_\beta = (1, \hat{S}_{x'}, \hat{S}_{y'}, \hat{S}_{z'})$  represent the target and recoil polarization vectors, respectively. These quantities are defined in the electron-plane coordinates (unprimed system) and hadron-plane coordinates (primed system) shown in Fig. 2.

Table 7 shows which response functions survive for various polarization conditions of the incident electron, target proton, and recoiling hyperon. In total, of the possible 144 terms in the full expansion of eq(14), only 36 independent, non-vanishing response functions are necessary to describe the electroproduction of pseudoscalar mesons. The remaining terms vanish due to CPT symmetry considerations, or are related to other response functions that do not vanish.

In general, the surviving response functions are present in two classes,  $R_L$ ,  $R_T$ ,  $R_{TL}$ , and  $R_{TT}$ , which are independent of the incident electron-beam helicity, and  $R_{TL'}$  and  $R_{TT'}$ , which are dependent on the electron-beam helicity. The left superscripts on the response functions,  $c$  or  $s$ , refer to whether the response function is multiplied by a cosine or a sine term, respectively. Note that because the hyperon spin vector is defined in a coordinate system that is rotating with respect to the laboratory, there are implicit dependencies on  $\theta_K^*$  and  $\phi_K^*$  in addition to those shown in eq(14) that require detailed considerations.

### 10.2 Hadrodynamic-Model Calculations

The hadrodynamic calculations included in Figs. 9 and 10 were carried out using the computer code of Mart that is described in Ref.[23]. In the figures, the columns labeled ‘‘Model’’ correspond to different hadrodynamic model choices that correspond to: Adelseck and Wright-1998 (solid), Cotanch (short dash, small gap), Williams-1992 (medium dash), Adelseck and Saghai-1990 (short dash, large gap), Mart I (long dash), Mart II (dot-dash, small gap), and Mart III (dot-dash, large gap). The different Mart models employ different prescriptions

for gauge invariance. For these calculations, we have selected a dipole form factor for the Lambda and the  $KK^*\gamma$  transition form factor of Williams.

In the figures, columns labeled “ $\Lambda$  FFs” correspond to different  $\Lambda$  form factor choices that correspond to: dipole (solid), unity (short dash, small gap), Williams I (medium dash), Williams II (short dash, large gap), Williams III (long dash), and Goeke (dot-dash). For these calculations, we have selected the model Williams-1992 and the  $KK^*\gamma$  transition form factor of Williams.

In the figures, columns labeled “Kaon FFs” correspond to different  $KK^*\gamma$  transition form factor choices that correspond to: VDM (solid), Muenz (short dash), and Williams (medium dash). For these calculations, we have selected the model Williams-1992 and the  $\Lambda$  form factor of Goeke.

Polarized Beam and Polarized Recoil										
$\beta$	$\alpha$	T	L	$cTL$	$sTL$	$cTT$	$sTT$	$cTL'$	$sTL'$	$TT'$
-	-	$R_T^{00}$	$R_L^{00}$	$R_{TL}^{00}$	0	$R_{TT}^{00}$	0	0	$R_{TL'}^{00}$	0
$x'$	-	0	0	0	$R_{TL}^{x'0}$	0	$R_{TT}^{x'0}$	$R_{TL'}^{x'0}$	0	$R_{TT'}^{x'0}$
$y'$	-	$R_T^{y'0}$	‡	‡	0	‡	0	0	‡	0
$z'$	-	0	0	0	$R_{TL}^{z'0}$	0	$R_{TT}^{z'0}$	$R_{TL'}^{z'0}$	0	$R_{TT'}^{z'0}$
Polarized Target										
-	x	0	0	0	$R_{TL}^{0x}$	0	$R_{TT}^{0x}$	$R_{TL'}^{0x}$	0	$R_{TT'}^{0x}$
-	y	$R_T^{0y}$	$R_L^{0y}$	$R_{TL}^{0y}$	0	‡	0	0	$R_{TL'}^{0y}$	0
-	z	0	0	0	$R_{TL}^{0z}$	0	$R_{TT}^{0z}$	$R_{TL'}^{0z}$	0	$R_{TT'}^{0z}$
$x'$	x	$R_T^{x'x}$	$R_L^{x'x}$	$R_{TL}^{x'x}$	0	‡	0	0	$R_{TL'}^{x'x}$	0
$x'$	y	0	0	0	‡	0	‡	‡	0	‡
$x'$	z	$R_T^{x'z}$	$R_L^{x'z}$	‡	0	‡	0	0	‡	0
$y'$	x	0	0	0	‡	0	‡	‡	0	‡
$y'$	y	‡	‡	‡	0	‡	0	0	‡	0
$y'$	z	0	0	0	‡	0	‡	‡	0	‡
$z'$	x	$R_T^{z'x}$	‡	$R_{TL}^{z'x}$	0	‡	0	0	$R_{TL'}^{z'x}$	0
$z'$	y	0	0	0	‡	0	‡	‡	0	‡
$z'$	z	$R_T^{z'z}$	‡	‡	0	‡	0	0	‡	0

Table 7: Response functions for pseudoscalar meson production [41]. The target (recoil) polarization is indicated by  $\alpha$  ( $\beta$ ). The last three columns are for when the electron is polarized. ‡ indicates a response function which does not vanish but is related to other response functions.

### 10.3 Elastic Cross Section

Presently the analysis of the 1.6 GeV elastic  $ep$  CLAS data have undergone the closest scrutiny with regard to the extracted cross sections. The discussion in this section will show our present ability to measure a cross section over a reasonably broad  $Q^2$  range for the case of elastic scattering [42]. As well, the single  $\pi^+$  and  $\pi^0$  electroproduction data have been presented at several international physics conferences and have shown excellent agreement with the existing world data [43, 44].

The analysis of the  $ep$  data has been carried out with both the CLAS measured inclusive and exclusive elastic cross sections summed over a series of data runs. The raw yields have been corrected with a CLAS fiducial-based acceptance function determined from our GSIM/GEANT Monte Carlo and have been corrected for contributions from the liquid hydrogen target walls.

The  $ep$  cross section as a function of polar angle for one of the CLAS sectors (sector 1) is shown in Fig. 41. This figure shows that the inclusive and exclusive cross sections are essentially indistinguishable, and agree well with the radiated Mott cross section [39]. There are still some problems at forward angles ( $\theta < 25^\circ$ ) which are suspected to have arisen from non-uniformities of the acceptance within our fiducial cut. The results clearly indicate, at least for the  $ep$  data, that the absolute scale of the cross sections is in excellent agreement (to a level better than 5%) over most of the acceptance region. These results are quite encouraging for the kaon analysis program.

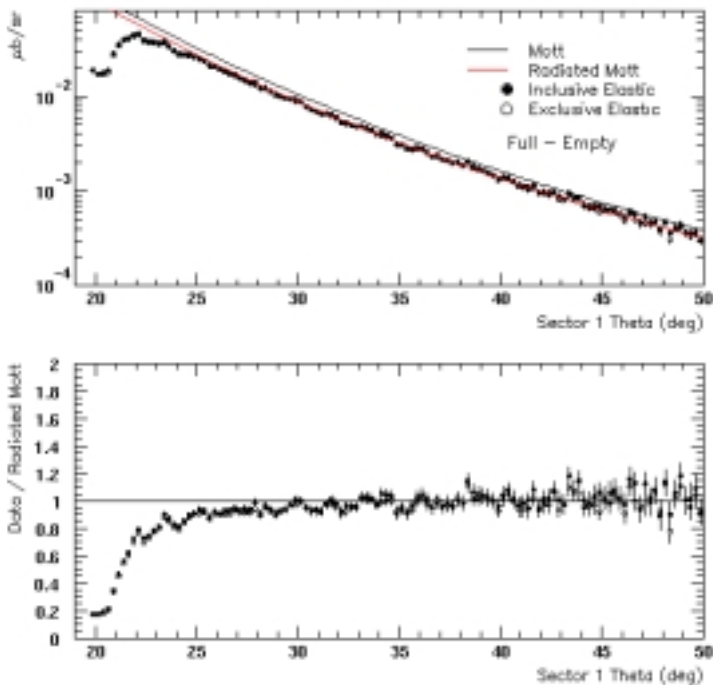


Figure 41: A comparison of the CLAS 1.645 GeV inclusive and exclusive elastic cross sections with the radiated Mott cross section as a function of polar angle.

## 10.4 Simple Quark Model

To estimate the counting rates for this experiment, we have used the published  $d\sigma_v/d\Omega_K^*$  electroproduction data from Bebek [18] (included in Fig. 25) as our starting point. These data span  $Q^2$  from 1.2 to 3.5 (GeV/c)<sup>2</sup>,  $W$  from 2.1 to 2.7 GeV, and  $\epsilon$  from 0.35 to 0.94. This data was limited to  $\theta_K^* < 15^\circ$ , or about 1.7% of the total solid angle. To estimate the value of the cross section at each of our  $Q^2/W$  points, we have employed a simple quark model to extrapolate from the Bebek data set, and we have employed a calculation from Bennhold to estimate  $\sigma_v^{tot}$  from  $d\sigma_v/d\Omega_K^*$  [45]. Our calculated total cross sections were then scaled by a factor to constrain the total rates over all  $Q^2/W$  bins to agree with the hyperon production rates measured in CLAS at 5.56 GeV.

The simple quark model employed assumed that the unpolarized virtual photon cross section could be written as:

$$\frac{d\sigma_v^{QM}}{d\Omega_K^*} = \frac{4\pi^2\alpha}{W^2 - M^2} \cdot \left[ \frac{4}{9}u_v(x) \right] f_k. \quad (15)$$

In this expression  $u_v(x)$  represents the  $u$ -quark momentum distribution in the proton (which we have taken as  $4(1 - x_B)^4$  [46]) and  $f_k$  is the probability that the final hadronic state is  $K\Lambda$  (which we take as 5% independent of  $W$  above threshold). Using the  $t$ -dependence of the differential cross section from calculations of Bennhold allows us to estimate that the  $15^\circ$  cut contained about 7.5% of the total events. With this factor, the total virtual photon cross section calculated for each  $Q^2/W$  bin is given by:

$$\sigma_v^{tot} = \frac{d\sigma_v^{QM}}{d\Omega_K^*} \cdot 4\pi \cdot \frac{0.0175}{0.075} \cdot N_d, \quad (16)$$

where  $N_d$  represents the scaling factor applied to all bins to match the overall production rate determined from analysis of 5.56 GeV CLAS data ( $N_d = 0.4$ ). For the rate estimates, we have assumed flat acceptances for the  $e'K^+$  and  $e'K^+p$  final states of 20% and 5%, respectively. Both of these assumptions are in reasonable agreement with our Monte Carlo (see Section 7). This acceptance factor includes not only the geometric acceptance of CLAS, but also accounts for the in-flight decay of kaons before they reach the outer scintillation counters.

## References

- [1] K.H. Hicks, M.D. Mestayer *et al.*, JLab Experiment E93-030.
- [2] L. Dennis, H. Funsten *et al.*, JLab Experiment E89-043.
- [3] D.S. Carman, K. Joo, L. Kramer, B.A.Raue *et al.*, JLab Experiment E99-006.
- [4] J.C. David, C. Fayard, G.H. Lamot, and B. Saghai, Phys. Rev. C **53**, 2613 (1996); T. Mizutani, C. Fayard, G.H. Lamot, B. Saghai, Phys. Rev. C **58**, 75 (1998).
- [5] R.A. Williams, C. Ji, and S.R. Cotanch, Phys. Rev. C **46**, 1617 (1992).
- [6] T. Mart, C. Bennhold, and C.E. Hyde-Wright, Phys. Rev. C **51**, 1074 (1995).
- [7] C. Bennhold, H. Haberzettl, and T. Mart, Preprint nucl-th/9909022, (1999); T. Mart and C. Bennhold, Phys. Rev. C **61**, 012201 (2000).
- [8] M.Q. Tran *et al.*, Phys. Lett B **445**, 20 (1998).
- [9] B. Saghai, Preprint DAPNIA-SPHN-00-24, Apr 2000.
- [10] G. Niculescu *et al.*, Phys. Rev. Lett. **81**, 1805 (1998).
- [11] S. Capstick and W. Roberts, Phys. Rev. D **58**, 74011 (1998).
- [12] E.S. Ackleh, T. Barnes, and E.S. Swanson, Phys. Rev. D **54**, 6811 (1996).
- [13] A. LeYaouanc *et al.*, Phys. Rev D **8**, 2223, (1973); Phys. Rev. D **9**, 1415, (1974); Phys. Rev. D **11**, 1272, (1975).
- [14] C. Bennhold, from talk presented at Workshop on Strange Quarks in Hadrons, Nuclei, and Nuclear Matter, Ohio University, Athens, Ohio, May 12-13, 2000.
- [15] F.X. Lee *et al.*, Preprint nucl-th/9907119, (1999).
- [16] M. Guidal *et al.*, Phys. Rev. C **61**, 025204, (2000).
- [17] M. Vanderhaeghen *et al.*, Phys. Rev. C **57**, 1454, (1998); M. Guidal *et al.*, Nucl. Phys. A **627**, 645 (1997).
- [18] C.J. Bebek *et al.*, Phys. Rev. D **15**, 3082 (1977).
- [19] R. Williams, private communication, (2000).
- [20] C.J. Bebek *et al.*, Phys. Rev. D **17**, 1693 (1978).
- [21] M.I. Adamovich *et al.*, Z. Phys. A **350**, 379 (1995).
- [22] J.E. Amaro and T.W. Donnelly, Annals of Phys. **263**, 56 (1998).
- [23] T. Mart and C. Bennhold, Nucl. Phys. A **639**, 237 (1998).

- [24] J.J. Kelly, Preprint nucl-th/9906049, (1999).
- [25] H. Schmieden and L. Tiator, Preprint nucl-th/9909046, (1999).
- [26] N. Isgur and G. Karl, Phys. Rev. D **23**, 817 (1981).
- [27] D.B. Lichtenberg, Phys. Rev. **178**, 2197 (1969).
- [28] C. Bennhold, from talk presented at HYPJLAB99, Workshop on Hypernuclear Physics with Electromagnetic Probes, Hampton, Virginia, Dec. 2-4, 1999.
- [29] T. Feuster and U. Mosel, Phys. Rev. C **59**, 460 (1999).
- [30] H. Haberzettl, C. Bennhold, T. Mart, and T. Feuster, Phys. Rev. C **58**, R40 (1998).
- [31] N. Levy *et al.*, Nucl. Phys. **55**, 493 (1973).
- [32] J.M. Laget, private communication, (1998).
- [33] K. Ackerstaff *et al.*, Eur. Phys. J. **C2**, 49 (1998).
- [34] J.W. Alcock *et al.*, Z. Phys. C **25**, 161 (1984); S. Kumano and V.R. Pandharipande, Phys. Rev. D **38**, 146 (1988).
- [35] T. Barnes, private communication, (1998).
- [36] J. Ellis, D. Kharzeev, and A. Kotzinian, Z. Phys. C **69**, 467 (1996).
- [37] B.Q. Ma and J. Soffer, Phys. Rev. Lett. **82**, 2250 (1999).
- [38] B.Q. Ma *et al.*, Preprint hep-ph/0005210, (2000).
- [39] Computer program of R. Minehart, unpublished, (1999).
- [40] N.C.R. Makins, Ph.D. Dissertation, MIT (1994).
- [41] G. Knöchlein, D. Drechsel, L. Tiator, Z. Phys. A **352**, 327 (1995).
- [42] Analysis of elastic  $ep$  cross sections done by L.C. Smith, (1999).
- [43] Analysis of  $ep \rightarrow en\pi^+$  data being carried out by K. Joo.
- [44] Analysis of  $ep \rightarrow ep\pi^0$  data being carried out by H. Egiyan.
- [45] K.H. Hicks, M.D. Mestayer *et al.*, JLab Proposal for E93-030, (1993).
- [46] A. Bodek, Ph.D thesis, Massachusetts Institute of Technology (1972).